Calcium isotope fractionation during melt immiscibility and carbonatite petrogenesis

M.A. Antonelli, G. Sartori, A. Giuliani, E.A. Schauble, J. Hoffmann, M.W. Schmidt

Supplementary Information

The Supplementary Information includes:

1. Centrifuging piston-cylinder experiments

Experiments on coexisting immiscible carbonatite and nephelinitic alkaline silicate melts were carried out using a centrifuging piston-cylinder apparatus (Schmidt *et al.*, 2006). This apparatus allows for near-perfect physical separation of two immiscible melts (**Fig. 1a**, **Fig. S-1**). The single-stage piston cylinder has a 14 mm bore, straight graphite heaters, a talc-pyrex-graphite-MgO assemblage, and a B-type Pt-Rh thermocouple. The experiments aim to equilibrate a mixture of a completely depolymerized silicate melt with a carbonatitic melt in order to understand if there would be any Ca isotope fractionation between an at least partly covalent silicate melt and an ionic carbonatic liquid. For the 1170 °C experiments, the starting material is a single bulk

composition corresponding to a 60:40 nephelinite:carbonatite mixture described in (Lee and Wyllie, 1998) and adapted by (Martin *et al.*, 2013), who obtained liquid immiscibility for this composition (**Table S-1**). The 800 °C experimental composition was based on previous work that successfully achieved liquid immiscibility at this temperature (Veksler *et al.*, 2012). The starting powders were dried overnight to remove adsorbed water, following the experimental routine of Martin *et al.* (2013).

Starting powders (~2 g) were made by mixing known quantities of analytical grade SiO_2, Al_2O_3, $Al(OH)_3$, Fe_2O_3, Fe_2SiO_4, MgO, $CaCO_3$, Na_2CO_3, $Na(OH)$, K_2CO_3, and $NaHPO_4$, with bulk compositions corresponding to those reported in **Table S-1** [Note that non-negligible Ca blanks during the experimental preparation procedure would have no bearing on our results because we measured the differences between two immiscible melts that formed from a single homogeneous powder (*i.e.*, the $\delta^{44}Ca$ difference between the two melts would not be affected if the sample were contaminated with exogenous calcium)]. After thorough homogenization, the powders (~30 mg per capsule) were tightly filled into 4x6 mm $Au_{80}Pd_{20}$ capsules. After heating to the target temperature (~45 minutes), the two resultant immiscible melts were equilibrated for 6 hours at 1170 °C and at pressures of 0.3, 0.8, and ~1.2 GPa (GS8-32, GS8-33, and GS8-34, respectively), and then mechanically separated by centrifuging at 1000 g for > 2 hours. The lower temperature experiment (GS9-37 at 800 °C, 0.8 GPa) was conducted analogously to the higher temperature experiments.

The experimental temperature gradient between the center and edge of the capsules is less than 6-9 °C (Hin *et al.*, 2012). Given that the temperature gradients are symmetric about the center of the capsule and that we fully dissolved each half (minus the interface and edges), any minor Soret effects (affecting either melt) should be canceled out. This inference agrees with our experimental results, where the 800 °C experiment [which has a smaller temperature gradient between the center and ends of the capsule (due to temperature scaling) compared to the higher temperature experiments] yields essentially the same $1000\ln\alpha_{carb-sil}$ (1000 K) value (within ~0.01‰) as the 1170 °C experiments.

After quenching, a thin longitudinal slice of the capsule was prepared for imaging (**Fig. S-1**) and major element analyses (**Table S-1**). Most of the near-perfectly separated carbonatitic quench and the silicate glass (*e.g.,* **Fig. 1a**) were mechanically extracted from the remainder of the capsule using a precision diamond wire saw and file, which resulted in two solid blocks (each with silicate glass and quenched carbonatite, to be broken in a tungsten carbide die). The interface between the two melts was removed and discarded, leading to small blocks of silicate glass (1 – 12 mg) and quenched carbonatitic melt (1-8 mg) from each experiment which were then dissolved for Ca isotope analyses by TIMS.

We targeted three different pressures in our 1170 °C experiments to control the amount of Ca in the silicate *vs*. carbonatite melt [F(Ca)] in order to demonstrate closed-system equilibrium behavior without having to change the composition of the starting materials (**Fig. S-3**). The experimental composition used in our lower-T (800 °C) experiment only produces coexisting immiscible carbonatite and silicate melts in a small P-T window, such that we did not explore pressure variations for the lower T experiment. Our current set of experiments covers the high- and low-temperature limits of carbonatite-silicate melt immiscibility. The observation that we get the same $1000\ln\alpha_{carb-sil}$(1000 K) from all four experiments, suggests that the carbonatite-silicate melt Ca isotope fractionation factor is well constrained by the present dataset.

2.   Ca isotope Analyses by Thermal-Ionization Mass Spectrometry (TIMS)

The silicate glass samples were dissolved using concentrated HF + 6M HCl (5:2 ratio) and refluxed in Savillex beakers for ~1 week at 130 °C, whereas the carbonatite quench samples were dissolved in 6M HCl for ~24 hours in order to leave behind any silicate glass particles that could have remained in the quenched carbonatite side after centrifugation. We did not, however, observe any visible residues in the carbonatitic samples after dissolution. For one silicate sample (GS9-37-silicate), we observed a slight fizz upon our initial addition of 6M HCl (prior to adding HF), and so we decanted this acid after ~10 minutes (at room temperature) and restarted with fresh HCl three times. No fizzing was observed afterwards, so we then proceeded with our

typical dissolution process for silicates. After evaporation, the samples were redissolved in 3 M HNO_3 for subsequent TIMS analyses using well-established methods (Antonelli *et al.*, 2019c, 2019b, 2023a, 2023b) described below.

2a. Radiogenic Ca isotope analyses

Approximately 30 μg of calcium were separated from dissolved samples using column chemistry methods (DGA resin, 3M HNO_3, and ultrapure H_2O) that are based on extensive previous work (*e.g.,* Antonelli *et al.*, 2019a, 2021a, 2023b). For each analysis, ~5 μg of unspiked Ca (in 3M nitric acid) was loaded onto zone-refined Re filaments, evaporated, coated with ~1-2 μL of 40 % phosphoric acid and heated to a dull red glow in a dark room before loading into the Triton-plus TIMS at ETH-Zurich. We used a double-filament method and heated samples slowly (<50 mA/min) in order to achieve stable ^{40}Ca signals of 20-30 volts. ^{42}Ca, ^{43}Ca, and ^{41}K were measured in faraday cups connected to 10^{13} Ω amplifiers, applying a response-time (Tau) correction, and ^{40}Ca and ^{44}Ca was measured on 10^{11} Ω amplifiers. The detailed analytical protocol is reported in Antonelli *et al.* (2021a). Resultant $^{40}Ca/^{44}Ca$ ratios were corrected to $^{42}Ca/^{44}Ca$ = 0.31221 with an exponential mass law (Russell *et al.*, 1978) and are reported as ε$_{Ca}$ values {defined as 10,000 x $[(^{40}Ca/^{44}Ca)_{sample}/(^{40}Ca/^{44}Ca)_{standard}$ -1]} relative to bulk-silicate Earth (BSE), which is defined by contemporaneous measurements of the USGS standard W-2a [best-estimated absolute $^{40}Ca/^{44}Ca$ = 47.157 (Antonelli *et al.*, 2021a)]. None of the samples had detectable levels of ^{39}K or ^{41}K after column chemistry.

Within the single analytical session from which all of the radiogenic Ca data in this study were obtained, SRM915a yielded an ε$_{Ca}$(BSE) value of +1.4 ± 0.4 (n = 1) relative to W-2a (n = 3), in agreement with previous work (**Table S-5**). The ε$_{Ca}$(BSE) value of carbonatite standard COQ-1 was found to be 0.4 ± 0.4 (n = 3), suggesting that it is indistinguishable from the BSE value and also agreeing with previous work within uncertainty (He *et al.*, 2017; Dai *et al.*, 2022). We also analyzed apatite and calcite separates from two of our carbonatite samples (SI-156 and X-1513) that were explicitly chosen because they represent the highest and

lowest δ^{44}Ca values found in our study (*see* **Fig. 2**). We found no resolvable difference in any of their ε_{Ca} compositions. Calcite and apatite from SI-156 have ε_{Ca}(BSE) of 0.4 ± 0.5 (n = 3) and those from X-1513 have ε_{Ca}(BSE) of 0.4 ± 0.3 (n = 3). Both of these values are the same as that of COQ-1 and within uncertainty of W-2a.

All of the above-quoted ε_{Ca}(BSE) uncertainties are a combination of the 2sd measurement uncertainties on both W-2a and on the analyzed sample (square root of the sum of the squared uncertainties). Although it is analytically challenging to distinguish between pure mantle calcium [ε_{Ca}(BSE) = 0] and calcium that may contain some marine carbonates [average ε_{Ca}(BSE) = 1.1 ± 0.3 (Antonelli *et al.*, 2021a)], our radiogenic Ca data are consistent with purely mantle-derived calcium in the sources of carbonatites. The uncertainties are too large, however, for this to be a particularly useful observation (*i.e.* they are within error of up to ~80% average marine carbonate).

2b. Stable Ca isotope analyses

Stable Ca isotope data were obtained by TIMS at the University of Bern, Switzerland (Thermo Scientific Triton plus), using the same dissolved sample solutions as for our radiogenic Ca measurements. The resultant δ^{44}Ca data [defined as $(^{44}Ca/^{40}Ca)_{sample}/(^{44}Ca/^{40}Ca)_{standard}-1$] are reported relative to Bulk Silicate Earth (BSE) in per mil notation (‰), where BSE has a recommended δ^{44}Ca value of +0.95 ‰ relative to SRM915a (Antonelli and Simon, 2020).

Column chemistry methods are the same as described for the radiogenic Ca measurements, except that a ^{42}Ca-^{48}Ca double-spike is added to the dissolved rock solutions prior to Ca separation to monitor potential fractionations during column chemistry and instrumental mass fractionation (IMF). This double spike is well-calibrated and is the same as used in previous stable Ca isotope studies (Antonelli *et al.*, 2019b, 2019c, 2023b). After Ca separation (~30 μg), samples were loaded in the same fashion as for our ε_{Ca} measurements but were analyzed at the University of Bern because the TIMS at ETH-Zurich does not have enough low-resistance

amplifiers (10^{11} Ω) to accommodate the enriched ^{42}Ca and ^{48}Ca in the double spike. The TIMS at the University of Bern benefits from an additional cup (L5) that allows for the simultaneous collection of ^{40}Ca (10^{11} Ω), ^{41}K (10^{12} Ω), ^{42}Ca (10^{11} Ω), ^{43}Ca (10^{12} Ω), ^{44}Ca (10^{11} Ω), ^{47}Ti (10^{12} Ω), and ^{48}Ca (10^{11} Ω) in static mode, but we also monitored ^{47}Ti with an electron multiplier in a second line of each measurement. We heated samples slowly to obtain stable (slowly-growing) ^{40}Ca signals of 7-9 volts. All samples [other than MC-1901 (apatite) and KS-2001 (calcite)] were analyzed a minimum of two times. Each analysis consisted of 100 cycles and each cycle consists of ten 1-second integrations (line 1), 5 seconds of downtime, and two 1-second integrations of ^{47}Ti on the SEM (followed by 3 seconds of downtime). We found that none of our analyses required corrections for possible isobaric interferences on ^{40}Ca (from ^{40}K) or ^{48}Ca (from ^{48}Ti).

Our measurements of dolerite standard W-2a and carbonatite standard COQ-1 give δ^{44}Ca$_{BSE}$ values of -0.13 ± 0.04‰ (2SE, n = 9) and -0.21 ± 0.03‰ (2SE, n = 5) in agreement with previously reported values for both standards (Banerjee *et al.*, 2021; Sun *et al.*, 2021; Zhao *et al.*, 2022; Antonelli *et al.*, 2023a, 2023b). Based on our nine W-2a measurements, we thus estimate that our internal 2SE uncertainty on δ^{44}Ca is ± 0.04 ‰, which happens to be the same value as our calculated repeatability (average absolute difference between duplicate measurements of 0.042 ‰) considering the 22 samples that were analysed twice in this study (**Table S-2**).

It has been recently suggested that tSE (rather than 2SE) better represents uncertainties for smaller groups of samples, such as those in typical stable isotope studies (Wang *et al.*, 2023). Our tSE uncertainty for W-2a is ± 0.047 ‰ (8 degrees of freedom at 95 % confidence) and for COQ-1 is 0.041 ‰ (4 degrees of freedom at 95 % confidence, **Table S-2**). Both of these uncertainties are very similar to our repeatability and to the 2SE uncertainty estimate of 0.04 ‰. These values in turn yield an estimated 2σ internal uncertainty of ± 0.06 ‰ for Δ^{44}Ca values (square root of the sum of squared uncertainties for δ^{44}Ca), which agrees well with the highly repeatable Δ^{44}Ca$_{carb-sil}$ values measured in our three high-T (1170 °C) experiments [Δ^{44}Ca values of -0.10 ‰ (0.3 GPa), -0.12 ‰ (0.8 GPa), and -0.08 ‰ (1.2 GPa)]. Given their higher degree of accuracy, we

report tSE uncertainties for averages derived from populations with n > 3, such as our calculated carbonatite-silicate melt fractionation factor (n = 4) and the average values for calcite (n = 8), apatite (n = 7), and all natural data from this study (n = 15), as well as for data from previous studies.

For our individual samples (most of which were analysed twice, as is often done by TIMS), the use of tSE (where t = 12.71 for a C.I. of 95 % with 1 degree of freedom) leads to a pronounced over-estimation of our uncertainties that are over an order of magnitude higher (tSE of up to ± 0.65 ‰) than our repeatability. This is likely because each single analysis entails 100 ten-second measurements, for a total of 200 ten-second analyses per sample measured in duplicate (*i.e.*, the effective n is > 2). This same number of analyses is equivalent to what would be referred to as 10 separate measurements by MC-ICP-MS [*e.g.*, for the measurements in (Antonelli *et al*., 2021b) performed at IPGP], so the decision on what to use as the true number of analyses for calculating tSE (or 2SE) is somewhat subjective and can vary from lab to lab. Thus, we argue that our internal uncertainty estimates for individual samples are best represented by those derived from our repeated standard measurements for W-2a and COQ-1 (where 2SE ≈ tSE ≈ 0.04 ‰), which give uncertainties that are highly consistent with our calculated repeatability.

We thus chose these internal uncertainties (± 0.04 ‰ for $\delta^{44}Ca$ and ± 0.06 ‰ for $\Delta^{44}Ca$) as the error bars to display in our figures (Fig. 1 and Fig. 2), as they should accurately reflect 2σ uncertainty in the measured isotopic differences between samples. Long-term external uncertainties, as estimated from repeated analyses of USGS standard W-2a by the lead author at the University of Bern over three years (n = 21, nine of which are reported in this study), on the other hand, are estimated to be ± 0.12 ‰ (2SD), which should be taken as the conservative uncertainty when comparing our $\delta^{44}Ca$ results to data from previous and future studies.

In addition to providing stable Ca isotope data, our double-spike Ca isotope analyses also give (isotope-dilution based) Ca concentrations in the analysed samples (**Table S-2**). These results agree quite well with the CaO concentrations determined by EPMA in the various minerals (**Table S-4**) and in the experimental silicate

and carbonatitic melts (**Table S-1**) suggesting that Ca blanks were negligible with respect to the amount of Ca dissolved. Although the dissolved experimental samples in this study provided ample amounts of calcium (62 to 1509 μg) and did not present any significant analytical challenges, we do not have a quantitative measurement of the Ca blanks in the U-Pb lab at ETH-Zurich where the chemical separations were performed. Nevertheless, published and unpublished Ca isotope results from the lab have been verified by five independent labs in a number of previous studies (Antonelli *et al.*, 2019c, 2023b, 2023a). Calcium contamination in our samples would decrease the magnitude of observed isotopic fractionations in our experiments. Given that our isotope-dilution Ca concentration measurements give results in agreement with those measured *in-situ* by EPMA, however, it is considered unlikely that significant Ca contamination occurred.

3. Density functional theory (*ab-initio*) estimates

Mineral structures (displayed in **Fig. S-4**) for calcite ($CaCO_3$), dolomite [$CaMg(CO_3)_2$], and ankerite [$CaFe(CO_3)_2$], were modeled using the plane-wave density functional theory package Quantum Espresso (Giannozzi *et al.*, 2009) and pseudopotentials from version 1.5 of the GBRV library [http://www.physics.rutgers.edu/gbrv/, (Garrity *et al.*, 2014)]. The fractionation factors were calculated using well-established methods (Schauble *et al.*, 2006), where phonon frequencies for ^{40}Ca and ^{44}Ca-substituted crystals were calculated at non-zero phonon wave vectors and used to estimate reduced partition functions ratios (Urey, 1947). Reduced partition functions ratios (*aka*. 'RPFR' or '1000lnβ') for the three mineral structures (reported in **Table S-3**) were estimated from force constants and determined by numerical differentiation of the energies of perturbed structures in which a Ca atom is slightly displaced from its equilibrium position in three orthogonal directions (Bigeleisen and Mayer, 1947; Schauble, 2011; Antonelli *et al.*, 2019c, 2023b). A vibrational frequency scale-factor of 1.06 was assumed for all models using the PBE functional, based on comparison with phonon frequencies measured at high-symmetry wave vectors in lime

and fluorite (Elcombe and Pryor, 1970; Saunderson and Peckham, 1971). Force constants calculated by displacing Ca-atoms (for calcite and diopside) were scaled by the square of this factor (1.1236) and yield results that are comparable to the phonon-based estimates (*e.g.*, calcite 1000lnβ of 1.275 and 1.254 at 1000 K, for phonon-based and force-constant estimates, **Table 1**). The values used in our model calculations (force-constant estimates for calcite and diopside, and phonon-based estimates for dolomite and fluorapatite) are displayed in bold font in **Table 1**.

For all estimates, we used a gradient-corrected (GGA) density functional [PBE; (Perdew *et al.*, 1996)], which has been successfully employed in several previous studies (Schauble *et al.*, 2006; Méheut *et al.*, 2007; Griffith *et al.*, 2008; Antonelli *et al.*, 2019c, 2023b). Several other studies have also provided DFT estimates for Ca isotopes in mineral structures (Feng *et al.*, 2014; Huang *et al.*, 2019; Song *et al.*, 2019; Li *et al.*, 2022; Wang *et al.*, 2017a; Xiao *et al.*, 2022), based on local density approximation (LDA) functionals, but these are not directly comparable to the RPFRs used in this study. Nevertheless, LDA-based estimates also give inter-mineral 1000lnα values that are generally consistent with our PBE-based estimates (Wang *et al.*, 2017a; Xiao *et al.*, 2022). Our estimated calcite-dolomite fractionation factor (+0.06 ‰ at 1000 K), for example, generally agrees with (but is slightly smaller than) previous results based on LDA functionals (+0.10 ‰) (Wang *et al.*, 2017a). We find that calcite is slightly lighter than diopside (by -0.06 ‰ at 1000 K) and slightly heavier than fluorapatite (by +0.05 ‰ at 1000 K), in agreement with previous predictions based on LDA functionals (Wang *et al.*, 2017a, 2017b). Note that calcite is predicted to be slightly heavier (+0.03 ‰ at 1000 K) than clinopyroxene, if combining the diopside prediction from (Feng *et al.*, 2014) with the calcite prediction from (Wang *et al.*, 2017a), but predicted to be -0.03 ‰ if using the 1000lnβ values from (Wang *et al.*, 2017a, 2017b). Our calcite-apatite prediction also compares favorably with previous work [+0.07 ‰ at 1000 K, combining LDA predictions from (Wang *et al.*, 2017a; Xiao *et al.*, 2022)]. Recent work suggests that PBE (and other generalized gradient approximation, GGA) predictions, however, are generally more accurate for estimating Ca isotope fractionation factors, but a correction factor for combining LDA- and PBE-based RPFRs has also

been proposed (Xiao *et al.*, 2022). This correction-dependent combination is not necessary for the study at hand, however, as all the relevant minerals have self-consistent PBE-based predictions from this study and Antonelli *et al.* (2019c, **Table S-3**). Finally, it is important to note that our RPFR estimates for various melt compositions (**Table 1**) are tied to PBE-based *ab-initio* predictions and would need to be adjusted if used in future studies based on different types of *ab-initio* (*e.g.*, LDA) predictions.

In line with previous studies, we assume that the RPFR of CO_2-rich alkaline silicate melt is half-way between diopside and labradorite (Antonelli *et al.*, 2019b, 2021b, 2023a, 2023b; Antonelli and Simon, 2020; ; Zhu *et al.*, 2021; Soderman *et al.*, 2022). For carbonatitic melt, we assume that the RPFR is lower than this melt by -0.21 (**Table 1**), which implies that the RPFR of nephelinite/syenite is the same as for the CO_2-rich precursor melt, prior to carbonatite-silicate immiscibility. We also explored models, however, where the carbonatitic melt has a higher RPFR (lower than the precursor melt by -0.11). Given that the experimentally-constrained carbonatite-silicate melt $1000\ln\alpha$(1000 K) value is -0.21, this assumption implies that the nephelinite/syenite melts would have a higher RPFR (by approximately +0.11) than the CO_2-rich precursor melts (**Table 1**). This difference, however, does not lead to significantly different results in our four-stage model of carbonatite petrogenesis, because the absolute RPFR value of carbonatitic melt is only required for calculating Ca isotope fractionations during calcite/apatite accumulation (Step 4 in our four-step model). In our direct-melting model for magneisocarbonatites (see **Section 5** of the Supplementary Information), the differences in our model results for the two carbonatitic melt RPFR estimates are more significant, because the absolute RPFR of carbonatitic melt is required for both stages of the model (partial melting and dolomite/apatite accumulation). This leads, therefore, to relatively larger uncertainties associated with our two-stage (direct-melting) model results (**Fig. S-5**) compared to those from our four-stage model estimates (**Fig. 3**). It should also be noted that additional components (not included in our experiments) could possibly have minor effects on Ca-O bonds in carbonatitic melts. These effects would be largely subordinate, however, to the effects from the carbonate anions that dominate the melt. Typical carbonatites have 1-2 wt. % P_2O_5, so

only a very small fraction of Ca bonding sites would be affected by the presence of phosphate. F has even lower concentrations than P_2O_5, and Cl is negligible. The experiments contained 1 wt. % H_2O, and it is likely that natural carbonatite and nephelinite melts contain more than this, but this is not currently known.

4.   Natural Carbonatite samples and mineral separates

Apatite and calcite were separated from one magnesiocarbonatite and seven calciocarbonatite whole-rock samples from 7 different countries. These rocks were characterized in previous work (Sartori *et al.*, 2023) and include samples from Brava Island (Canary Islands), Sokli and Siilinjarvi (Finland), Phalaborwa (South Africa), Oka (Canada), Mount Weld (Australia), Marinkas Quellen (Namibia), and Kaiserstuhl (Germany). The magnesiocarbonatite sample (Marinkas Quellen) is the only one with disequilibrium calcite-apatite REE distributions (indicative of calcite recrystallization), whereas the calciocarbonatite samples all have equilibrium REE distributions indicative of a primary magmatic nature (Sartori *et al.*, 2023).

Briefly, the Brava island sample (X-1513, sövite dyke) consists of clusters of unaltered nephelinite with calcite and apatite inclusions, as well as clinopyroxene and magnetite in textural equilibrium with the calcite matrix. The Kaiserstuhl sample (KS-2001, olivine-bearing sövite) has decimeter-sized calcite comb-layers ascribed to rapid magmatic crystallization (observed at the outcrop scale). The Mount Weld sample (MW-2, biotite bearing sövite) consists of coarse-grained calcite matrix cross-cut by fine-grained biotite and apatite domains. The Oka sample (OKA-BZ2, niocalite bearing sövite) contains small apatite grains in a coarse calcite matrix. The Phalaborwa sample (PLBC-1) contains large apatite grains in a matrix of calcite, and shows granuloblastic structures in thin section, similar to our sample from Siilinjarvi (SI-156). The Sokli sample (SO-199) contains fresh (idiomorphic) biotite and apatite in a calcite matrix, and our magnesiocarbonatite sample from Marinkas Quellen (MC-19-01, beforsite) is composed almost exclusively of dolomite and minor apatite. Despite having disequilibrium REE signatures indicative of recrystallization in this sample (Sartori *et al.*, 2023), the slightly positive $\Delta^{44}Ca_{apatite-dolomite}$ (+0.05 ± 0.06 ‰) agrees with our equilibrium predictions

(**Fig. 2a, Table 1**). Whole-rock chemical data can be found in **Table S-3**. For more information (and photomicrographs) on these samples, see Sartori *et al.*, (2023).

Mineral separations were performed by hand picking using a binocular microscope, resulting in apatite grains with diameters of 100 to 1000 μm and calcite grains ranging in size from 250 to 1000 μm (**Table S-4**). Prior to dissolution, the mineral separates were weighed on a high-precision microbalance (typically used for weighing zircons at ETH-Zurich) and range from ~0.1 to 14 mg for apatite and ~2 to 16 mg for calcite (or dolomite, **Table S-2**). Other than for apatite from MC-19-01 (which could not be accurately weighed due to small sample size), the purity of our mineral separates and experimental samples was confirmed by isotope-dilution based Ca concentration measurements (see Section 2, **Table S-2**), which agree very well with *in-situ* measurements performed by EPMA (**Table S-4**).

5.   Two-stage (direct-melting) model for magnesiocarbonatites

We chose to evaluate the two principal petrogenetic models of carbonatite formation, namely (i) direct-melting of mantle carbonates and (ii) differentiation of a CO_2-rich alkaline silicate melt resulting in melt-immiscibility. A third model, which entails continuous differentiation of a CO_2-rich silicate melt until carbonatitic melt is formed (without any silicate-carbonatite immiscibility) is only applicable to the rare carbonatite bodies that are associated with kimberlites and ultramafic lamprophyres (*e.g.*, Dawson and Hawthorne, 1973; Smith *et al.*, 2013; Tappe *et al.*, 2017; Abersteiner *et al.*, 2019). These carbonatites represent a very small proportion of carbonatites in the world (Woolley and Kjarsgaard, 2008). Extensive differentiation of mantle-derived silicate melts to form carbonatitic melts without carbonatite-silicate liquid immiscibility requires mantle pressures and is considered a rare case not applicable to the vast majority of carbonatites. Due to its complexity (*e.g.*, continuous change of melt 1000lnβ during evolution from silicate to carbonatitic melt) and rareness, we have chosen to not model this process.

In **Fig. S-5** we show results for our two-stage (direct-melting) petrogenetic model for magnesiocarbonatites (*e.g.,* Harmer and Gittins, 1998; Yaxley and Brey, 2004). Based on observations from carbonated mantle xenoliths [up to 2-3 wt. % carbonates (*e.g.,* Ionov *et al.*, 1996)], we conservatively assume that 1-5 wt. % carbonate (dolomite, 21 wt. % Ca) with $\delta^{44}Ca_{BSE}$ of 0 ‰ (≈ BSE, red), -0.35 ‰ [average Phanerozoic marine carbonate (Fantle and Tipper, 2014), orange], or -0.67 ‰ [100-200 Ma marine carbonate average (Banerjee *et al.*, 2021), blue] is first mixed into the mantle source (garnet lherzolite, **Fig. S-5b**). The source then undergoes incongruent partial melting where all the carbonates melt and the generated carbonatitic melt equilibrates isotopically with the residual mantle minerals [using the minimum and maximum 1000lnβ values for garnet lherzolite mantle sources (Antonelli *et al.*, 2023a)].

The absolute RPFR (1000lnβ value) of carbonatitic melt is poorly constrained, so we show model results for 1000lnβ values of 0.929 (as discussed in the main text, "low melt RPFR") and of 1.037 ("high melt RPFR") at temperatures of 950-1050 °C, which is the minimum melting temperature for carbonated mantle lithosphere (Foley and Pintér, 2018). To account for the full range of possible $\delta^{44}Ca$ values, we (i) pair the maximum mantle-source RPFR with the "low melt RPFR" estimate and lower temperature limit (thus yielding the largest possible fractionations), and (ii) pair the minimum mantle-source RPFR with the "high melt RPFR" estimate and higher temperature limit (yielding the smallest possible fractionations, **Fig. S-5c**).

Given that 100 % of the carbonates melt during partial melting, the F(Ca) value (*i.e.* the Ca fraction retained by the residual mantle minerals after melting) is fully controlled by the amount of carbonates initially added to the mantle source, where greater amounts of incorporated carbonate lead to lower F(Ca) because more carbonatitic melt is generated (**Fig. S-5c**). This behavior, which has not been considered in most previous models, thus serves to *increase* the $\delta^{44}Ca$ of generated melts when greater amounts of carbonate are present in the mantle source. We find that, if the $\delta^{44}Ca_{BSE}$ value of the incorporated carbonates is higher than the predicted negative fractionation factor for partial melting (*e.g.*, carbonates with $\delta^{44}Ca_{BSE} > -0.25$ ‰), adding more carbonates into the mantle source actually increases the $\delta^{44}Ca$ of the directly-generated carbonatitic melts

(through a decrease in F(Ca), as shown in **Fig. S-5c**). This behavior changes when the carbonate $\delta^{44}Ca_{BSE}$ value is equal to the fractionation factor for partial melting [yielding melts with invariant composition, regardless of the F(Ca), when assuming closed-system equilibrium], and behaves as expected (*i.e.* lowering the $\delta^{44}Ca$ of carbonatitic melts) when the carbonate $\delta^{44}Ca_{BSE}$ is lower than the melt-mantle fractionation factor. In essence, adding more carbonates to the mantle source only lowers $\delta^{44}Ca$ of carbonatitic melts *if* the carbonates have $\delta^{44}Ca_{BSE} < 1000\ln\alpha_{melt\text{-}mantle}(T)$ (in the closed-system case), otherwise, carbonate addition actually increases the $\delta^{44}Ca_{BSE}$ of generated carbonatitic melts through a feedback with F(Ca) during partial melting, even if the incorporated carbonates have nominally lower $\delta^{44}Ca$ than the mantle.

After partial melting, the equilibrated melt rises into the upper crust and crystallizes dolomite at 1000-800 °C [likely entailing 70-90 % crystallization, where $K_d(Ca)$ for dolomite-melt ≈ 1], leading to slightly heavier $\delta^{44}Ca$ in the cumulates relative to the carbonatitic melts. As in the first stage of this model, we paired the higher temperature limit for crystallization (1000 °C) with the higher carbonatitic melt RPFR estimate and the lower temperature limit (800 °C) with the lower melt RPFR estimate, in order to recreate the full range of possible values for the dolomite cumulates (+0.01 ‰ to +0.12 ‰ heavier than the carbonatitic melt, **Fig. S-5d**). Note that apatite has essentially the same RPFR as dolomite (**Table 1**), so the estimates would not be noticeably different if apatite is included in the crystallizing mineral assemblage.

The net effect of these two sequential processes leads to predicted magnesiocarbonatite compositions that generally agree with natural data (**Data S-1**), with $\delta^{44}Ca_{BSE}$ ranging from -0.41 ‰ to -0.05 ‰ when assuming that the mantle source has 1-5 wt. % dolomite (*e.g.,* Dasgupta and Hirschmann, 2006) with $\delta^{44}Ca_{BSE}$ = 0 (**Fig. S-5e**). Thus, we predict similar $\delta^{44}Ca$ ranges for magnesiocarbonatite cumulates that are derived through differentiation of initially calciocarbonatitic melts (*i.e.,* when enough calcite precipitates to saturate dolomite, in our four-stage model) and those that are derived from primary magnesiocarbonatitic melts formed through direct melting of carbonate-bearing mantle.

Using the two lower $\delta^{44}Ca$ values for carbonates (depicted in orange and blue in **Fig. S-5**) leads to predicted carbonatite values of -0.46 ‰ to -0.15 ‰ (1-5 wt. % dolomite with $\delta^{44}Ca_{BSE}$ = -0.35 ‰, orange) and -0.55 ‰ to -0.17 ‰ (1-5 wt. % dolomite with $\delta^{44}Ca_{BSE}$ = -0.67 ‰, blue). Although these estimates have a larger uncertainty than those associated with our four-stage model in the main text (due to the highly variable dolomite mode in mantle sources and that our absolute carbonatitic melt RPFR estimate come into play in both the accumulation *and* partial-melting stages), the natural data are best reproduced when using carbonates with $\delta^{44}Ca$ = BSE. The two lower carbonate $\delta^{44}Ca$ values considered in our model calculations [-0.35 ‰, corresponding to average Phanerozoic marine carbonates (Fantle and Tipper, 2014), and -0.67 ‰, corresponding to average 100-200 Ma marine carbonates (Banerjee *et al.*, 2021)] lead to predicted magnesiocarbonatite $\delta^{44}Ca$ compositions that are mostly lower than those observed in nature (**Fig. S-5e**).

6. Four-stage melt-immiscibility model for calciocarbonatites (and magnesiocarbonatites)

The first stage, low-degree partial melting of carbon-bearing garnet lherzolite to form a CO_2-rich alkaline (ultra)mafic melt, was explored in a recent study (Antonelli *et al.*, 2023a). To remain conservative, we take the minimum and maximum fractionation factors from that study and assume that temperatures for initial partial-melting range between 1400-1300 °C *e.g.,* (Foley and Pintér, 2018). Given that the degrees of melting are very low, the melt compositions can be approximated by the mineral-melt fractionation factors, leading to $\delta^{44}Ca_{BSE}$ values between -0.13 ‰ and -0.18 ‰ (**Fig. 3e**), when starting from bulk-mantle with $\delta^{44}Ca_{BSE}$ = 0 ‰ [equivalent to +0.95 ‰ relative to NIST SRM915a (Antonelli and Simon, 2020)]. These estimates agree very well with the average $\delta^{44}Ca_{BSE}$ composition of kimberlites [-0.16 ± 0.03 ‰ (Antonelli *et al.*, 2023a)], which are likely to be similar to the melts generated in the first stages of carbonatite formation.

The second stage, fractionation of minerals from the primitive melt, is then required to reach carbonatite-silicate two-melt immiscibility and can occur via two different pathways (Schmidt and

Weidendorfer, 2018). The first path leads to coexisting carbonatite + nephelinite (or similar) melts ("path 1"), and the second leads to carbonatite + foidic syenite melts ("path 2"). The first path entails 20-30 % fractional crystallization with an olivine to clinopyroxene ratio of 4:1 and temperatures of 1300-1000 °C [estimated from (Weidendorfer *et al.*, 2016)], yielding F(Ca) values of ~0.9 [*i.e.* ~90 % of Ca stays in the melt, assuming that clinopyroxene-melt K_d(Ca) ≈ 2, **Fig. 3b**]. The second path is assumed to occur over the same temperature range but entails 80-90 % fractional crystallization of olivine and clinopyroxene, with some alkali-feldspar in the latest stages (Schmidt and Weidendorfer, 2018), leading to F(Ca) values conservatively ranging between 0.5 and 0.3 (~30 wt. % clinopyroxene removal, **Fig. 3b**). We assume that the 1000lnβ(1000K) of CO_2-rich alkaline mafic melt is 1.144, as previously inferred for carbonated silicate melts (such as kimberlites, **Table 1**) and typical basaltic melts at lower pressures (Soderman *et al.*, 2022; Antonelli *et al.*, 2023a). The 1000lnβ(1000K) of diopside is 1.311 (Antonelli *et al.*, 2019c, 2021b; Eriksen and Jacobsen, 2022; Soderman *et al.*, 2022), whereas olivine and alkali-feldspars have insufficient calcium to significantly affect Ca isotopes in the differentiated melt. Clinopyroxene fractionation thus yields estimated δ^{44}Ca shifts in the residual melts (considering both closed-system, where the melt and crystals stay in equilibrium, and open-system behaviour, where the crystals are removed from the system) ranging from -0.01 ‰ to -0.02 ‰ for path 1 and from -0.03 ‰ to -0.12 ‰ for path 2 (**Fig. 3b,e**).

The third stage, where the CO_2-rich silicate melt separates into an immiscible carbonatite and nephelinite or foidic syenite melt, typically leads to ≤5 % carbonatite (based on the CO_2 mass-balance during liquid immiscibility – see below). Given the relatively low solubility of CO_2 in alkaline and silica-undersaturated melts (such as nephelinite) at subvolcanic pressure and temperature conditions (Morizet *et al.*, 2014), the likely maximum amount of carbonatitic melt that can be exsolved is ~7 wt. %, but may be significantly less when considering the limiting effects of other chemical components. From our experiments and comparisons of average CaO in bulk carbonatites, nephelinites, and syenites from the EarthChem database and previous studies (Supplementary **Data S-3**) typical carbonatite-nephelinite and carbonatite-syenite K_d(Ca)

values are 2-4 (Weidendorfer *et al.*, 2016) and 6-20 (Weidendorfer and Asimow, 2022), respectively. CO_2 solubility in syenite melt, on the other hand, is 2-6 times lower than in nephelinite melts at identical pressure (Brooker *et al.*, 2001; Morizet *et al.*, 2002). This suggests that, on average, smaller quantities of carbonatitic melt are exsolved from syenitic vs. nephelinitic melts, which serves to counteract the higher $K_d(Ca)$ for carbonatite-syenite and leads to conservative F(Ca) values of 0.9 to 0.8 for immiscibility stemming from both paths (*i.e.* 10-20 % of the Ca budget goes into the carbonatitic melts, **Fig. 3c**).

Our argument for the relative proportions of carbonatite and conjugate silicate melts formed during immiscibility does not stem from observations of natural outcrops, which are unlikely to mirror primary silicate/carbonatite melt proportions. Carbonatitic melts migrate upward through the crust more effectively than silicate melts (due to high buoyancy and low viscosity compared to silicate melts) and should thus physically decouple from their conjugate silicate melts. The outcrop level of natural carbonatite complexes thus has little bearing on relative magma volumes. To reiterate, our proportion of possible carbonatite stems from the solubility of CO_2 in alkaline silicate melts [*e.g.*, for a syenitic melt this is 0.3-1.0 wt. % CO_2 at 5-15 kbar (Morizet *et al.*, 2002)]. Carbonatites have 30-40 wt. % CO_2 thus suggesting that 1 to 4 wt. % carbonatite would be formed if all CO_2 were to go into a carbonatitic melt. A portion of the CO_2, however, remains in the silicate melt, so only a fraction of this maximum prediction would be formed. For nephelinites, CO_2-solubility at 15 kbar is ~4 times higher than for syenites, so more carbonatitic melt could theoretically be unmixed from nephelinitic melts. This difference is unlikely to significantly affect the predicted F(Ca) values, however, given that the larger quantity of unmixed carbonatite is essentially canceled out by the lower Ca distribution coefficient [$K_d(Ca)_{carb-neph}$] compared to that for carbonatite-syenite (see above). Our estimate of up to 5 wt. % carbonatitic melt, therefore, represents a number at the uppermost possible end when looking at CO_2 solubility in silicate melts in the middle- to lower-crust. We argue that immiscibility happens in the lower to mid-crust, below the outcrop levels, yet, if immiscibility were to happen at the subvolcanic levels of many carbonatite

outcrops, much less than 1 % of carbonatite would form, as CO_2 solubility in silicate melts at 1-2 kbar is <<1 wt. % (Brooker and Kjarsgaard 2011 *and references therein*).

Taking the best-fit fractionation factor from our experiments (-0.21 ‰ at 1000 K) and assuming temperatures of 1100-1000 °C for immiscibility (Brooker and Kjarsgaard, 2011; Weidendorfer and Asimow, 2022; Berkesi *et al.*, 2023) leads to estimated $\delta^{44}Ca$ shifts of -0.09 ‰ to -0.12 ‰ in the carbonatitic melt (relative to the parental CO_2-rich alkaline melt from stage 2) when considering both open- and closed-system behaviours (**Fig. 3c**) and regardless of the melt differentiation pathway.

The fourth stage, accumulation of calcite (and apatite) to form calciocarbonatite intrusives, typically occurs at temperatures of ~1000-800 °C and entails 70-90 % crystallization [equivalent to 10-30 wt. % loss of an alkali-rich carbonatitic melt (Sartori and Schmidt, 2023)] with a calcite-carbonatite melt $K_d(Ca)$ of 1.2-1.6 (Weidendorfer *et al.*, 2017). These constraints yield estimated F(Ca) values ranging from approx. 0.2 to 0.0 (*i.e.* 80 to almost 100 % of the total Ca ends up in the cumulates, **Fig. 3d**). The absolute $1000ln\beta$ of carbonatitic melt, however, cannot be directly constrained from our experiments, as we measure only the difference between carbonatite and nephelinite melts. We assume, therefore, that the nephelinite(/syenite) melts have the same $1000ln\beta$ as the parental melt (1.144 at 1000 K) and that the carbonatitic melt value is lower by -0.21 [yielding an estimated $1000ln\beta(1000 K)$ of 0.929, **Table 1**]. Combining the carbonatitic melt estimate with our *ab-initio* calculations (where calcite is slightly heavier than fluorapatite), we find that the predicted $\delta^{44}Ca$ shift in the pooled cumulates, relative to the initial carbonatitic melt, likely ranges from 0.00 ‰ to +0.11 ‰ (**Fig. 3d**). Given that the absolute $1000ln\beta$ of carbonatitic melt is poorly constrained, we also evaluated model results using a higher RPFR value {1.037 at 1000 K, which is higher than our preferred estimate by [0.5 x $1000ln\alpha(1000 K)_{carbonatite-silicate}$]}, but this yields only slightly less positive, yet essentially the same, $\delta^{44}Ca$ values in the final cumulates ($\Delta^{44}Ca$ from 0 to +0.08 ‰, for Step 4). This higher β value for carbonatitic melt, however, would also require that the nephelinite melt has a higher β value, such that the $1000ln\beta$ difference between them stays the same ($1000ln\alpha$ of -0.21 at 1000 K). We consider this unlikely

because the structure (Ca bonding environment) of the CO_2-depleted nephelinite/syenite melt after immiscibility is probably not drastically different from the Ca bonding environment in the melt prior to immiscibility.

Once enough Ca (roughly estimated as ~80 %) is removed, the differentiated melt becomes sufficiently enriched in Mg to crystalize dolomite (*i.e.* when F(Ca) < 0.2), possibly leading to the formation of differentiated magnesiocarbonatites. Given that residual carbonatitic melt has lower $\delta^{44}Ca$ after calcite precipitation (**Fig. 3d**) and that dolomite has a slightly lower $1000\ln\beta$ than calcite, we predict that magnesiocarbonatites should have lower $\delta^{44}Ca$ (by at least ~0.1 ‰) than genetically-related calciocarbonatites.

Although other Ca-bearing minerals have been observed in some carbonatites, garnet is rare in CO_2-rich alkaline precursor magmas that can evolve to silicate-carbonatite melt immiscibility, because garnet crystallization requires high Al/(Na+K) while immiscible silicate melts are alkaline. Perovskite is a groundmass phase that crystallizes relatively late in these magmas and only occurs in the most silica-undersaturated cases. If they occur at all, these minerals crystallize mainly as late accessories and would not contain more than ~1 wt. % of the total Ca budget, thus having negligible effects on magmatic Ca isotope compositions of carbonatites. Garnet and perovskite are therefore not considered in our models other than residual garnet during partial melting of garnet lherzolite (stage 1).

Adding together the maximum and minimum $\delta^{44}Ca$ estimates from the four sequential stages of our model (**Fig. 3e,** Supplementary **Data S-2**) leads to calciocarbonatite cumulates with estimated $\delta^{44}Ca_{BSE}$ ranging between -0.32 ‰ and -0.12 ‰, for those derived from nephelinites ('path 1' in **Fig. 3**), and from -0.43 ‰ to -0.14 ‰, for those derived from foid-syenites ('path 2'). In the context of our model, we find that the additional isotopic fractionation resulting from melt-immiscibility (Step 3) can explain calciocarbonatite $\delta^{44}Ca_{BSE}$ values <-0.2 ‰ (in nephelinite-derived carbonatites) and <-0.3 ‰ (in syenite-derived carbonatites), suggesting that immiscibility is a key process in the petrogenesis of many carbonatites.

Finally, ferrocarbonatites are thought to be derived from pervasive carbothermal and/or hydrothermal alteration (*e.g.,* Pirajno *et al.*, 2014). Their slightly higher δ^{44}Ca values (**Fig. 3e**) suggests that secondary alteration may push δ^{44}Ca to heavier values. Whether precipitated kinetically or at isotopic equilibrium, calcite is predicted to be isotopically lighter than aqueous Ca (Tang *et al.*, 2008; DePaolo, 2011; Brown *et al.*, 2013; Fantle and Tipper, 2014; Mills *et al.*, 2021; Watkins and Antonelli, 2021). A positive shift in ferrocarbonatites, therefore, could occur through interactions with evolved fluids (*e.g.*, those that have previously precipitated isotopically light carbonates), but this does not necessarily indicate that hydrothermal alteration always leads to positive δ^{44}Ca shifts (*e.g.*, addition of hydrothermally precipitated carbonates could also lower δ^{44}Ca, depending on reaction rates and on the extents of Ca distilled from the fluids). It must be underlined that, in many carbonatite occurrences, large volumes are affected by carbothermal and hydrothermal alteration (Mitchell and Gittins, 2022). Thus, demonstration that carbonatite samples are truly magmatic (Sartori *et al.*, 2023), is required for meaningful interpretation of magmatic process or mantle-source variations.

7.   Comparisons with previous δ^{44}Ca data and other isotopic studies

We have shown that Ca isotope variations thus far observed in carbonatites do not require recycled marine carbonates in their mantle sources. This variability can instead be explained through magmatic processes accompanying the various stages of carbonatite petrogenesis, including carbonatite-silicate melt immiscibility, which we have experimentally shown leads to significant Ca isotope fractionation. Although previous work excluded melt-immiscibility as a source of δ^{44}Ca fractionations in carbonatites by using mass-balance arguments [which predicted δ^{44}Ca values far higher than observed in natural conjugate silicates (Banerjee *et al.*, 2021)], this was based on improbable assumptions, including (i) very low values for F(Ca), equivalent to 70-90% of the Ca going into the carbonatitic melts (*vs.* only 10-20 % in our model, see Fig. 3c) and (ii) that all of the fractionation required to explain the δ^{44}Ca of their samples occurred solely during carbonatite-silicate immiscibility (*i.e.*, bulk precursor melts have δ^{44}Ca = BSE when they reach the two-melt stability field).

Previous work looking at seventeen calcite separates in carbonatites (Banerjee *et al.*, 2021) found a significantly larger range of $\delta^{44}Ca$ values than observed here. The entire range of calcite $\delta^{44}Ca_{BSE}$ values that were observed (-0.4 ‰ to +0.3 ‰) can also be found within a single carbonatite complex (Oka, Canada). This strongly suggests that carbonatite $\delta^{44}Ca$ variations depend on processes, and not solely on their sources. There are several reasons why calcite grains may have a range of $\delta^{44}Ca$ values, including primary magmatic processes, such as those occurring during step 4 of our model (calcite accumulation). During this accumulation stage, early-formed calcite may have $\delta^{44}Ca$ values up to approx. +0.3 ‰ higher than its parental carbonatitic melt, and late-formed (instantaneous) calcite may potentially have very negative values at low F(Ca) values (see Fig. 3d). Therefore, these calcite signatures could potentially be manifested through open-system processes such as melt loss. Thus, $\delta^{44}Ca$ variations, even amongst primary calcite grains, are not unexpected. Secondary alteration processes may also influence calcite and appear to typically push $\delta^{44}Ca$ to higher values (Banerjee *et al.*, 2021; Sun *et al.*, 2021).

Here, we found only a very limited range of calcite $\delta^{44}Ca$ values. All of our calcite and apatite samples, other than apatite in one sample (X-1513 from Brava), have $\delta^{44}Ca_{BSE}$ values that lie within < 0.1 ‰ of the average of our samples (-0.30 ‰). The primary magmatic nature of our samples has been strongly confirmed by previous work (Sartori *et al.*, 2023). Given that essentially all these samples give the same $\delta^{44}Ca$, we could claim that this value represents the unaltered signature of primary carbonatites. On the other hand, we have only analyzed minerals from eight samples, so it will be crucial to analyze more thoroughly-characterized mineral separates from fresh carbonatites with primary magmatic signatures in future work to better our understanding of Ca isotope variability in calcite.

By using our experimentally constrained carbonatite-silicate melt fractionation factor and including the effects of both partial melting and fractional crystallization into our four-stage petrogenesis model, we successfully explained the Ca isotope compositions of carbonatites from our study and from previous work, without appealing to mantle source variations. Previous studies modeling Ca isotope fractionations during

carbonatite petrogenesis, however, used significantly different parameters in their models (Banerjee *et al.*, 2021; Sun *et al.*, 2021). For example, Sun *et al.* (2021) assumed a garnet-melt fractionation factor [$1000\ln^{44/40}\alpha$ (1000 K)] of +1.15 ‰ (equivalent to $\Delta^{44/42}Ca_{grt-melt}$ = +0.56 ‰), whereas Banerjee *et al.* (2021) used a garnet-melt fractionation factor of +0.66 ‰ (1000 K), based on *ab-initio* (LDA-based) estimates for grossular garnet from (Huang *et al.*, 2019). Here, we use *ab-initio* (PBE-based) predictions for pyrope (Antonelli *et al.*, 2019c), as this is the dominant garnet end-member in the mantle, yielding a $1000\ln\alpha_{grt-melt}$ (1000 K) = +0.89 ‰. This fractionation factor also assumes that the $1000\ln\beta$ value for primordial CO_2-rich silicate melt is half-way between PBE-based *ab-initio* estimates of diopside and plagioclase (An50), as suggested from studies of kimberlites (Antonelli *et al.*, 2023a) and discussed earlier in the supplement. Another notable difference is that the models in Sun *et al.* (2021) assume an initial mantle $\delta^{44}Ca_{915a}$ composition of +0.88 ‰ (corresponding to $\delta^{44}Ca_{BSE}$ of -0.07 ‰) instead of the generally accepted value of +0.95 ‰ [$\delta^{44}Ca_{BSE}$ = 0 ‰ (Kang *et al.*, 2017; Antonelli and Simon, 2020)].

Although we successfully explain the $\delta^{44}Ca$ of carbonatites with sequential equilibrium magmatic processes, it remains possible that the $\delta^{44}Ca$ of carbonatites could be influenced by high temperature diffusive-kinetic effects [*e.g.*, Zhao *et al.*, 2017; Antonelli *et al.*, 2019b, 2019c, 2023b; Antonelli and Simon, 2020; Kang *et al.*, 2020; Watkins and Antonelli, 2021]. In future studies, triple Ca isotope analyses ($\Delta^{48}Ca'$) will yield especially important information regarding the Ca isotope fractionation mechanisms (*i.e.*, equilibrium *vs.* diffusive-kinetic effects) that operate during formation of carbonatites. All the processes that we model in this study assume Ca isotope equilibrium between the various minerals and melt phases. Our models would be confirmed, therefore, by $\Delta^{48}Ca'$ values of ~0 ppm [*i.e.*, confirming adherence to an equilibrium mass law (Antonelli *et al.*, 2019c)]. Triple Ca isotope values ($\Delta^{48}Ca'$) adhering to an equilibrium mass law would thus be entirely consistent with our model calculations and would have no bearing on the presence of recycled marine carbonates in the sources of carbonatites.

For the reasons made explicit throughout this manuscript, stable Ca isotopes are not ideal tracers of sedimentary carbonates in the mantle. Paired with other geochemical proxies, however, Ca isotopes may be used in future studies to better understand a number of factors (*e.g.*, source-rock mineral assemblage; extents of partial melting, fractional crystallization, and melt-immiscibility) involved in carbonatite formation. Calcium isotopes should also yield similar process-dependent information for carbonatites formed through direct partial melting of mantle carbonates, and potentially on the $\delta^{44}Ca$ of their carbonate sources, but future efforts need to focus on better understanding the many processes that can undoubtedly modify the $\delta^{44}Ca$ of mantle-derived magmas.

Beyond Ca isotopes, a number of non-traditional stable isotope systems have been used to help understand the origins of carbonatite magmas, including B (Hulett *et al.*, 2016; Çimen *et al.*, 2018, 2019; Kuebler *et al.*, 2020), Mg (Li *et al.*, 2016; Su *et al.*, 2019), Fe (Johnson *et al.*, 2010), and Ba isotopes (Li *et al.*, 2020). A majority of the studies investigating isotopic variations of the heavier elements (*e.g.*, Mg, Fe, Ba) in carbonatites suggest that isotopic variations can be explained by various magmatic processes, and do not require incorporation of recycled marine carbonates (Johnson *et al.*, 2010; Li *et al.*, 2016, 2020; Su *et al.*, 2019).

The slightly positive boron isotope compositions (*i.e.*, $\delta^{11}B$ up to approx. +5 ‰ *vs.* approx. -7 ‰ for the mantle) of < 300 Ma carbonatites, however, have been ascribed to increased recycled marine carbonates in the mantle-sources of carbonatites at this point in Earth history (Hulett *et al.*, 2016). Although the number of data used to draw this conclusion were quite limited [*e.g.*, only five Precambrian data points, two of which actually have the same (slightly high) $\delta^{11}B$ values as the < 300 Ma carbonatites], subsequent location-specific studies also adopted a similar interpretation (Çimen *et al.*, 2018, 2019; Kuebler *et al.*, 2020). In addition to the lack of heavy carbon isotope signatures in the samples from Hulett *et al* (which would be expected if marine carbonates were involved), we argue that these slightly heavy boron isotope signatures do not serve as unequivocal evidence for recycled marine carbonates in the sources of carbonatites. Ophiolites, altered oceanic

crust, and serpentinites all have high δ^{11}B values of up to +19 ‰, +25 ‰, and +41 ‰, respectively (Smith *et al.*, 1995; Vils *et al.*, 2009; Yamaoka *et al.*, 2012, 2015), and could also impart heavy δ^{11}B signatures, along with enriched ^{87}Sr/^{86}Sr isotope compositions, to carbonatite source rocks. Given that metabasites have been shown to retain essentially MORB-like Ca isotope compositions during prograde metamorphism (Lu *et al.*, 2019), mixing with AOC would be unlikely to significantly change the Ca isotope composition of the mantle-sources of carbonatites, and thus could potentially explain both Ca and B isotope observations (assuming that boron behaves as a perfect tracer). On the other hand, boron is a fluid mobile trace element and is heavily susceptible to fluid exsolution (Marschall, 2018, *and references therein*). It is uncertain, therefore, whether the boron isotope composition of carbonatites can be regarded as that of their original mantle sources, even if the carbonatites are minimally altered. Thus, it will be important for future work to focus on how magmatic processes and fluid exsolution from carbonatites [which can have a wide variety of chemical compositions (Walter *et al.*, 2021)] may influence boron isotope fractionation.

Supplementary Tables

Table S-1 Experimental melt compositions (by EPMA). All concentration data are reported in wt. %.

Sample	Material	T [°C]	P [kbar]	SiO_2	Al_2O_3	CaO	K_2O	FeO	Na_2O	MgO	P_2O_5	CO_2	H_2O	TOTAL
GS9	Starting material	-	-	37.96	6.30	4.20	16.29	0.00	13.78	0.72	0.00	19.75	1.00	100.00
-	-	-	-	-	-	-	-	-	-	-	-	-	-	-
GS9-37	Carb	800	8	0.06	-	7.53	22.45	-	25.43	0.12	-	-	-	55.59
-	-	-	-	0.03	-	0.59	2.95	-	0.86	0.06	-	-	-	-
GS9-37	Sil	800	8	58.21	6.70	4.32	16.74	0.05	11.09	0.83	-	-	-	97.95
-	-	-	-	0.53	1.78	0.47	0.58	0.01	1.17	0.03	-	-	-	-
GS8	Starting material	-	-	18.77	6.91	16.79	1.98	2.96	19.76	7.90	0.01	22.67	2.24	99.99
-	-	-	-	-	-	-	-	-	-	-	-	-	-	-

Table S-1 continued

Sample	Material	T [°C]	P [kbar]	SiO$_2$	Al$_2$O$_3$	CaO	K$_2$O	FeO	Na$_2$O	MgO	P$_2$O$_5$	CO$_2$	H$_2$O	TOTAL
GS8-34	Carb	1170	3	3.26	0.25	21.78	3.02	0.61	23.80	5.77	-	38.72	-	97.21
-	-	-	-	0.65	0.13	0.87	0.05	0.07	0.64	0.46	-	-	-	-
GS8-34	Sil	1170	3	32.76	13.09	14.83	1.31	2.67	14.37	8.35	-	6.71	-	94.09
-	-	-	-	10.17	3.65	1.26	0.19	0.20	0.33	0.16	-	-	-	-
GS8-33	Carb	1170	8	5.10	0.63	22.49	1.91	1.89	18.29	8.86	-	35.24	-	94.40
-	-	-	-	1.34	0.40	2.25	0.22	0.41	1.12	2.28	-	-	-	-
GS8-33	Sil	1170	8	38.66	16.26	8.61	1.91	4.07	14.12	4.96	-	14.74	-	103.31
-	-	-	-	0.99	0.41	0.42	0.02	0.06	0.10	0.17	-	-	-	-
GS8-32	Carb	1170	12	4.53	0.75	21.55	1.90	1.51	20.17	8.04	-	35.64	-	94.08
-	-	-	-	2.04	0.68	2.70	0.30	0.52	1.18	2.81	-	-	-	-
GS8-32	Sil	1170	12	39.10	16.14	8.62	1.86	4.30	14.47	5.10	-	6.93	-	96.51
-	-	-	-	1.19	0.26	0.44	0.02	0.10	0.18	0.13	-	-	-	-

Table S-2 Stable Ca isotope data. (Note: 2SD uncertainties reported here are the analytical uncertainties associated with each measurement (100 cycles of ten 1-second integrations per analysis).

Location	Sample	Type	Dissolved sample (mg)	δ^{44}Ca (BSE)	2SD	Average δ^{44}Ca(BSE)	Ca (wt. %)	2SD
Natural carbonatites								
Brava island (CV)	X-1513	calcite	9.14	-0.33	0.03	**-0.33**	40.5	1.0
				-0.33	0.03		40.5	1.0
	X-1513	apatite	1.85	-0.46	0.04	**-0.45**	39.7	1.0
				-0.45	0.03		39.7	1.0
Sokli (FI)	SO-199	calcite	10.27	-0.23	0.04	**-0.23**	38.8	0.9
				-0.22	0.04		38.8	0.9
	SO-199	apatite	14.19	-0.27	0.03	**-0.22**	39.7	1.0
				-0.17	0.03		39.7	1.0
Siilinjarvi (FI)	SI-156	calcite	13.16	-0.23	0.03	**-0.25**	37.3	0.9
				-0.26	0.03		37.3	0.9
	SI-156	apatite	13.17	-0.28	0.04	**-0.30**	39.8	1.0
				-0.32	0.03		39.8	1.0

Table S-2 continued

Location	Sample	Type	Dissolved sample (mg)	$\delta^{44}Ca$ (BSE)	2SD	Average $\delta^{44}Ca$(BSE)	Ca (wt. %)	2SD
Phalaborwa (SA)	PLBC-1	calcite	3.04	-0.31	0.03	**-0.30**	38.1	0.9
				-0.29	0.04		38.1	0.9
	PLBC-1	apatite	0.87	-0.40	0.04	**-0.36**	39.8	1.0
				-0.31	0.04		39.8	1.0
Oka (CA)	OKA-BZ2	calcite	15.90	-0.36	0.04	**-0.30**	38.9	0.9
				-0.23	0.03		38.9	0.9
	OKA-BZ2	apatite	1.00	-0.30	0.03	**-0.31**	35.1	0.8
				-0.33	0.04		35.1	0.8
Mount Weld (AUS)	MW-2	calcite	10.84	-0.28	0.04	**-0.30**	39.0	0.9
				-0.33	0.04		39.0	0.9
	MW-2	apatite	0.65	-0.32	0.04	**-0.28**	34.7	0.8
				-0.25	0.03		34.7	0.8
Marinkas Quellen (NM)	MC-19-1	dolomite	2.36	-0.28	0.03	**-0.31**	21.8	0.5
				-0.35	0.03		21.8	0.5
	MC-19-1	apatite	< 0.1	-0.26	0.11	**-0.26**	-	-
Kaiserstuhl (DE)	KS-2001	calcite	2.87	-0.28	0.03	**-0.28**	36.9	0.9
Experimental samples								
Starting Materials	GS9-SM	starting mat.	12.83	-0.30	0.03	**-0.30**	3.0	0.1
	GS8-SM	starting mat.	19.23	-0.32	0.04		11.6	0.3
				-0.27	0.03		11.6	0.3
800°C, 0.8 Gpa	GS9-37-Sil	silicate	12.31	-0.19	0.04	**-0.24**	2.9	0.1
				-0.28	0.03		2.9	0.1
	GS9-37-Carb	carbonatite	1.16	-0.43	0.03	**-0.43**	5.4	0.1
				-0.43	0.04		5.4	0.1
1170°C, 0.3 Gpa	GS8-34-Sil	silicate	6.48	-0.22	0.03	**-0.22**	11.3	0.3
				-0.22	0.03		11.3	0.3
	GS8-34-Carb	carbonatite	2.48	-0.30	0.04	**-0.32**	15.9	0.4
				-0.35	0.03		15.9	0.4
1170°C, 0.8 Gpa	GS8-33-Sil	silicate	1.11	-0.24	0.03	**-0.27**	7.3	0.2
				-0.31	0.04		7.3	0.2
	GS8-33-Carb	carbonatite	5.98	-0.40	0.04	**-0.39**	16.1	0.4
				-0.38	0.03		16.1	0.4
1170°C, 1.2 Gpa	GS8-32-Sil	silicate	2.87	-0.30	0.04	**-0.29**	6.6	0.2
				-0.28	0.03		6.6	0.2
	GS8-32-Carb	carbonatite	8.48	-0.40	0.04	**-0.37**	16.0	0.4
				-0.34	0.03		16.0	0.4

Table S-2 continued

Location	Sample	Type	Dissolved sample (mg)	$\delta^{44}Ca$ (BSE)	2SD	Average $\delta^{44}Ca$(BSE)	Ca (wt. %)	2SD
Standards								
Virginia, USA	W-2a	Diabase	-	-0.19	0.04	-	-	-
				-0.04	0.04	-	-	-
				-0.14	0.04	-	-	-
				-0.20	0.03	-	-	-
				-0.06	0.03	-	-	-
				-0.12	0.04	-	-	-
				-0.18	0.04	-	-	-
				-0.19	0.04	-	-	-
				-0.09	0.03	-	-	-
			Average	**-0.13**				
			2SE	**0.041**				
			tSE	**0.047**				
Oka, Canada	COQ-1	Carbonatite	**13.93**	**-0.20**	0.03	-	33.6	0.8
				-0.17	0.03	-	33.6	0.8
				-0.21	0.04	-	33.6	0.8
				-0.25	0.03	-	33.6	0.8
				-0.24	0.04	-	33.6	0.8
			Average	**-0.21**				
			2SE	**0.029**				
			tSE	**0.041**				

Table S-3 Natural carbonatite whole-rock chemical compositions.

Table S-3 is available for download from the online version of this article at

https://doi.org/10.7185/geochemlet.2338

Table S-4 Natural carbonatite apatite and calcite chemical compositions.

Table S-4 is available for download from the online version of this article at

https://doi.org/10.7185/geochemlet.2338

Table S-5 Radiogenic Ca isotope data. All measurements come from the same session (same barrel). *Combined uncertainties include measurement uncertainty on the samples and on W-2a (square root of the sum squared uncertainties). Corr. = mass-fractionation corrected to ^{42}Ca/^{44}Ca = 0.31221 using an exponential law.

name	40Ca/44Ca (corr.)	40Ca/42Ca (corr.)	43Ca/44Ca (corr.)	42Ca/44Ca (raw)	εCa(BSE)	2SD (combined)*	40/44Ca (norm. 47.157)
COQ-1	47.1547	151.0353	0.064883	0.3139	0.52		47.1594
COQ-1	47.1548	151.0356	0.064879	0.3150	0.53		47.1595
COQ-1	47.1536	151.0316	0.064881	0.3152	0.27		47.1583
COQ-1 Mean	47.1544	151.0342	0.064881	0.3147	**0.44**	*0.36*	47.1591
2sd	0.0014	0.0044	0.000004	0.0014	*0.29*		
SI156 - Apatite	47.1555	151.0379	0.064879	0.3138	0.69		47.1602
SI156 - Calcite	47.1542	151.0337	0.064883	0.3100	0.41		47.1589
SI156 - Calcite	47.1533	151.0308	0.064883	0.3138	0.22		47.1580
SI-156 Mean	47.1544	151.0341	0.064881	0.3126	**0.44**	*0.52*	47.1591
2sd	0.0022	0.0072	0.000005	0.0044	*0.47*		
X1513 - Apatite	47.1539	151.0326	0.064880	0.3143	0.34		47.1586
X1513 - Apatite	47.1541	151.0333	0.064880	0.3150	0.38		47.1588
X1513 - Calcite	47.1546	151.0349	0.064882	0.3147	0.49		47.1593
X-1513 Mean	47.1542	151.0336	0.064881	0.3147	**0.40**	*0.26*	47.1589
2sd	0.0007	0.0024	0.000003	0.0007	*0.16*		
SRM915a	47.1588	151.0483	0.064883	0.3100	**1.38**	*0.41*	47.1635
W-2a	47.1525	151.0283	0.064885	0.3137	0.05		47.1572
W-2a	47.1526	151.0286	0.064886	0.3144	0.07		47.1573
W-2a	47.1518	151.0258	0.064881	0.3131	-0.12		47.1564
W-2a Mean	47.1523	151.0275	0.064884	0.3137	**0.00**	*0.29*	47.1570
2sd	0.0010	0.0031	0.000006	0.0013	*0.21*		

Supplementary Datasets

Data S-1 Compilation of carbonatite δ^{44}Ca data from this and previous studies.

Data S-2 Rayleigh calculation results for carbonatite models.

Data S-3 Earthchem results for CaO in relevant rock-types.

Datasets S-1 to S-3 (.xlsx) are available for download from the online version of this article at https://doi.org/10.7185/geochemlet.2338

Supplementary Figures

Figure S-1 Back-scattered electron images of centrifuging piston-cylinder experimental run products. Quenched silicate melt (light grey), quenched carbonatitic melt (dark grey), palladium-gold capsule (white). Although we see a meniscus for other two-liquid immiscibility experiments (*e.g.,* silicate *vs.* metallic melt, silicate *vs.* sulfide melt, and two-silicate melts) performed in the centrifuging piston cylinder apparatus, this is not the case for carbonatite-nephelinite melt experiments. Though speculative, the CO_2-rich nephelinite melt may have too low of a viscosity (or unfavorable wetting properties) for the formation of a meniscus between carbonatite and nephelinite melts.
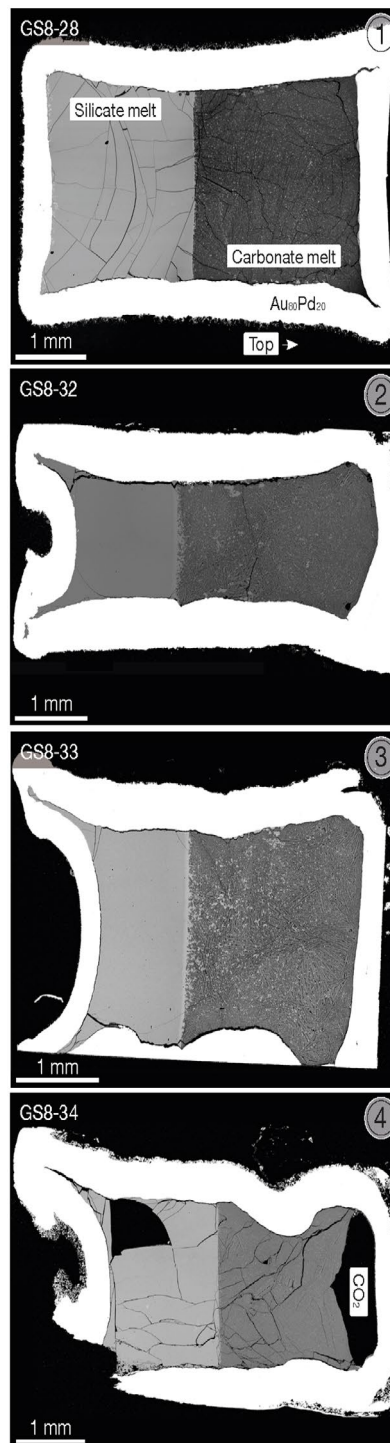
Figure S-2   Experimental melt compositions *vs.* carbonatite-silicate melt Ca isotope fractionation factors [1000lnα at 1000 K]. Fractionation factors were calculated using a $10^6/T^2$ law.
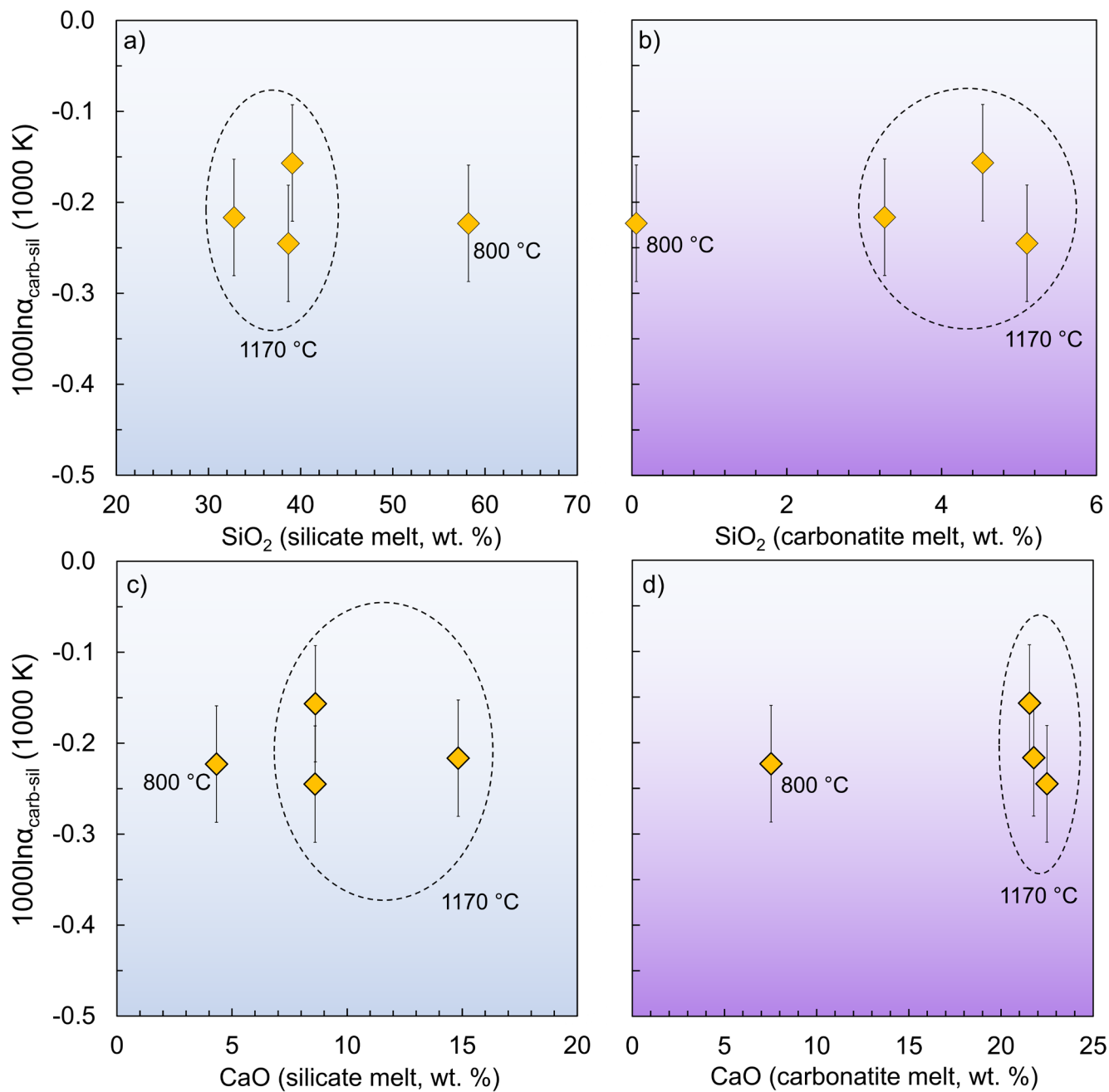
Figure S-3   Experimental δ^{44}Ca *vs.* F(Ca) for the 1170 °C experiments, compared with expected closed-system equilibrium behavior (dashed lines).

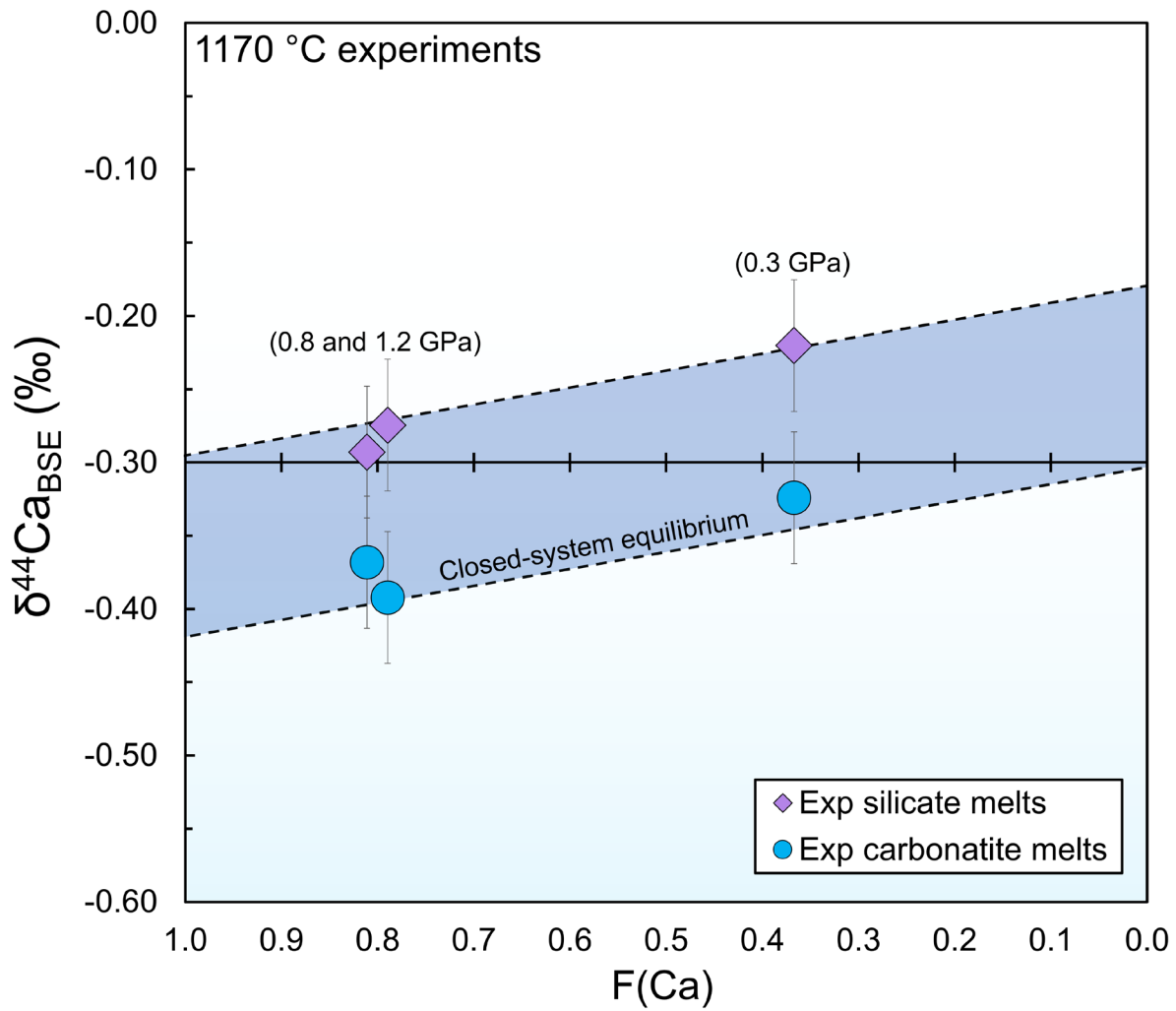**Figure S-4**   Mineral structures for **(a)** calcite, **(b)** dolomite, and **(c)** ankerite used in *ab-initio* estimates. Calcium atoms (blue octahedra), magnesium atoms (orange octahedra), iron atoms (brown octahedra), oxygen atoms (red spheres), carbon atoms (dark brown spheres). Images were generated using *Vesta* (Momma and Izumi, 2011). Average Ca-O bond lengths, coordinations, and 1000lnβ values are reported in **Table 1**.

a) Calcite ($CaCO_3$)   b) Dolomite [$CaMg(CO_3)_2$]   c) Ankerite [$CaFe(CO_3)_2$]
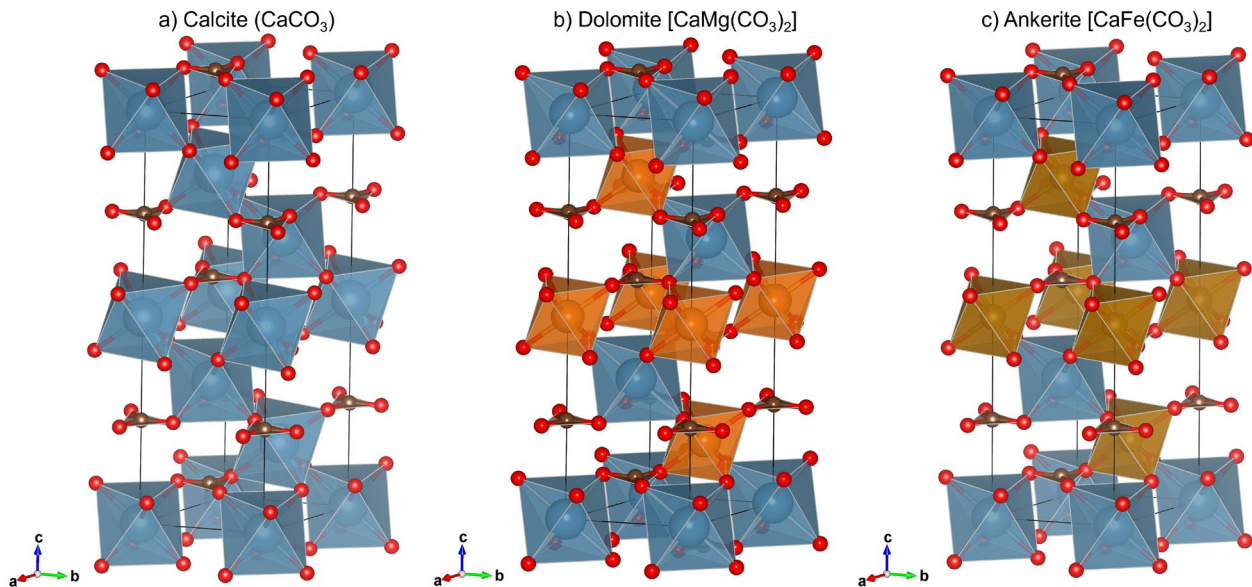
Figure S-5   Two-stage (direct-melting) petrogenetic model for magnesiocarbonatites. **(a)** fractionation factors for partial melting ('1') and dolomite fractionation ('2'). **(b)** Effect of mixing 1-5 wt. % carbonate (dolomite) into the mantle with $\delta^{44}Ca_{BSE}$ of 0 ‰ (≈ BSE, red), -0.35 ‰ (orange), or -0.67 ‰ (blue). **(c)** Estimates for Ca isotope fractionation during incongruent partial melting of carbonate-bearing mantle, where F(Ca) is the Ca fraction remaining in the solids. **(d)** Dolomite crystallization from carbonatitic melts at 1000-800 °C, leading to slightly heavier $\delta^{44}Ca$ in the cumulates, where F(Ca) is the Ca fraction remaining in the carbonatitic melt. Panel **(e)** shows the summative effects of these processes on the various source compositions, leading to predicted magnesiocarbonatite compositions that generally agree with natural data (**Data S-1**).
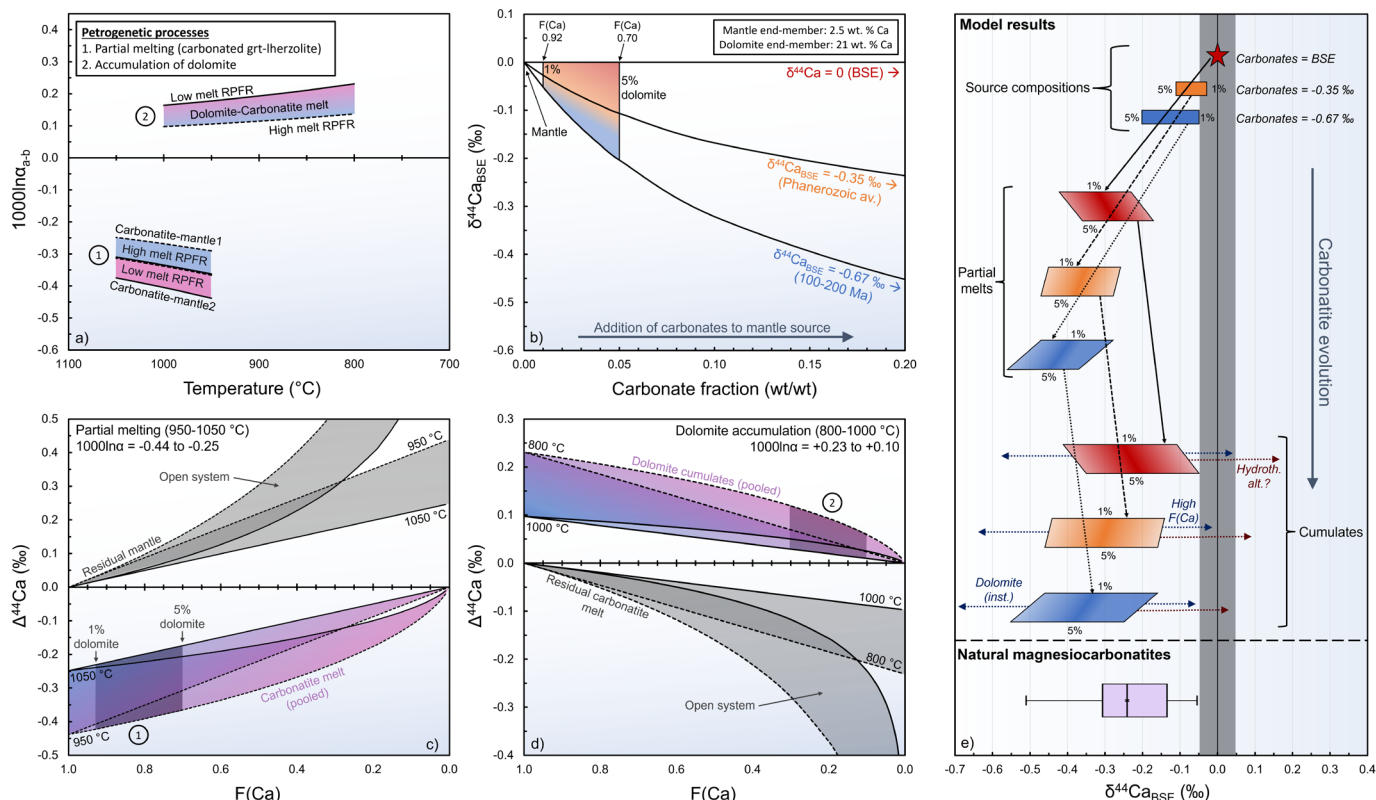
Supplementary Information References

Abersteiner, A., Kamenetsky, V.S., Goemann, K., Giuliani, A., Howarth, G.H., Castillo-Oliver, M., Thompson, J., Kamenetsky, M. and Cherry, A. (2019) Composition and emplacement of the Benfontein kimberlite sill complex (Kimberley, South Africa): Textural, petrographic and melt inclusion constraints. *Lithos*, *324*, 297-314. https://doi.org/10.1016/j.lithos.2018.11.017

Antonelli, M.A. Giuliani, A., Wang, Z., Wang, M., Zhou, L., Feng, L., Li, M., Zhang, Z., Liu, F. and Drysdale, R.N. (2023a) Subducted carbonates not required: Deep mantle melting explains stable Ca isotopes in kimberlite magmas. *Geochimica et Cosmochimica Acta* 348, 410–427. https://doi.org/10.1016/j.gca.2023.03.025

Antonelli, M.A., Yakymchuk, C., Schauble, E.A., Foden, J., Janoušek, V., Moyen, J.-F., Hoffmann, J., Moynier, F., Bachmann, O. (2023b) Granite petrogenesis and the δ^{44}Ca of continental crust. *Earth and Planetary Science Letters* 608, 118080. https://doi.org/10.1016/j.epsl.2023.118080

Antonelli, M.A., DePaolo, D.J., Christensen, J.N., Wotzlaw, J.-F., Pester, N.J., Bachmann, O. (2021a) Radiogenic ^{40}Ca in seawater: implications for modern and ancient Ca cycles. *ACS Earth and Space Chemistry* 5, 2481–2492. https://doi.org/10.1021/acsearthspacechem.1c00179

Antonelli, M.A., Kendrick, J., Yakymchuk, C., Guitreau, M., Mittal, T., Moynier, F. (2021b) Calcium isotope evidence for early Archaean carbonates and subduction of oceanic crust. *Nature Communications* 12, 2534. https://doi.org/10.1038/s41467-021-22748-2

Antonelli, M.A., Simon, J.I. (2020) Calcium isotopes in high-temperature terrestrial processes. *Chemical Geology* 548, 119651. https://doi.org/10.1016/j.chemgeo.2020.119651

Antonelli, M.A., DePaolo, D.J., Chacko, T., Grew, E.S., Rubatto, D. (2019a) Radiogenic Ca isotopes confirm post-formation K depletion of lower crust. *Geochemical Perspectives Letters* 9, 43–48. https://doi.org/10.7185/geochemlet.1904

Antonelli, M.A., Mittal, T., McCarthy, A., Tripoli, B., Watkins, J.M., DePaolo, D.J. (2019b) Ca isotopes record rapid crystal growth in volcanic and subvolcanic systems. *Proceedings of the National Academy of Sciences* 116, 20315–20321. https://doi.org/10.1073/pnas.1908921116

Antonelli, M.A., Schiller, M., Schauble, E.A., Mittal, T., DePaolo, D.J., Chacko, T., Grew, E.S., Tripoli, B. (2019c) Kinetic and equilibrium Ca isotope effects in high-T rocks and minerals. *Earth and Planetary Science Letters* 517, 71–82. https://doi.org/10.1016/j.epsl.2019.04.013

Banerjee, A., Chakrabarti, R., Simonetti, A. (2021) Temporal evolution of $\delta^{44/40}$Ca and ^{87}Sr/^{86}Sr of carbonatites: implications for crustal recycling through time. *Geochimica et Cosmochimica Acta* 307, 168–191. https://doi.org/10.1016/j.gca.2021.05.046

Berkesi, M., Myovela, J.L., Yaxley, G.M., Guzmics, T. (2023) Carbonatite formation in continental settings via high pressure – high temperature liquid immiscibility. *Geochimica et Cosmochimica Acta* 349, 41–54. https://doi.org/10.1016/j.gca.2023.03.027

Bigeleisen, J., Mayer, M.G. (1947) Calculation of Equilibrium Constants for Isotopic Exchange Reactions. *The Journal of Chemical Physics* 15, 261–267. https://doi.org/10.1063/1.1746492

Brooker, R., Kohn, S., Holloway, J., McMillan, P. (2001) Structural controls on the solubility of CO2 in silicate melts. *Chemical Geology* 174, 225–239. https://doi.org/10.1016/S0009-2541(00)00353-3

Brooker, R.A., Kjarsgaard, B.A. (2011) Silicate-carbonate liquid immiscibility and phase relations in the system SiO2-Na2O-Al2O3-Cao-Co2 at 0·1-2·5 GPa with applications to carbonatite genesis. *Journal of Petrology* 52, 1281–1305. https://doi.org/10.1093/petrology/egq081

Brown, S.T., Kennedy, B.M., DePaolo, D.J., Hurwitz, S., Evans, W.C. (2013) Ca, Sr, O and D isotope approach to defining the chemical evolution of hydrothermal fluids: Example from Long Valley, CA, USA. *Geochimica et Cosmochimica Acta* 122, 209–225. https://doi.org/10.1016/j.gca.2013.08.011

Çimen, O., Kuebler, C., Simonetti, S.S., Corcoran, L., Mitchell, R., Simonetti, A. (2019) Combined boron, radiogenic (Nd, Pb, Sr), stable (C, O) isotopic and geochemical investigations of carbonatites from the Blue River Region, British Columbia (Canada): Implications for mantle sources and recycling of crustal carbon. *Chemical Geology*, 119240. https://doi.org/10.1016/j.chemgeo.2019.07.015

Çimen, O., Kuebler, C., Monaco, B., Simonetti, S.S., Corcoran, L., Chen, W., Simonetti, A. (2018) Boron, carbon, oxygen and

radiogenic isotope investigation of carbonatite from the Miaoya complex, central China: Evidences for late-stage REE hydrothermal event and mantle source heterogeneity. *Lithos* 322, 225–237. https://doi.org/10.1016/j.lithos.2018.10.018

Dai, W., Moynier, F., Paquet, M., Moureau, J., Debret, B., Siebert, J., Gerard, Y., Zhao, Y. (2022) Calcium isotope measurements using a collision cell (CC)-MC-ICP-MS. *Chemical Geology* 590, 120688. https://doi.org/10.1016/j.chemgeo.2021.120688

Dasgupta, R., Hirschmann, M.M. (2006) Melting in the Earth's deep upper mantle caused by carbon dioxide. *Nature* 440, 659–662. https://doi.org/10.1038/nature04612

Dawson, J.B., and Hawthorne, J.B. (1973) Magmatic sedimentation and carbonatitic differentiation in kimberlite sills at Benfontein, South Africa. *Journal of the Geological Society*, *129*, 61-85. https://doi.org/10.1144/gsjgs.129.1.0061

DePaolo, D.J. (2011) Surface kinetic model for isotopic and trace element fractionation during precipitation of calcite from aqueous solutions. *Geochimica et Cosmochimica Acta* 75, 1039–1056. https://doi.org/10.1016/j.gca.2010.11.020

Elcombe, M.M., Pryor, A.W. (1970) The lattice dynamics of calcium fluoride. *Journal of Physics C: Solid State Physics 3, 492*. https://doi.org/10.1088/0022-3719/3/3/002

Eriksen, Z.T., Jacobsen, S.B. (2022) Calcium isotope constraints on OIB and MORB petrogenesis: The importance of melt mixing. *Earth and Planetary Science Letters* 593, 117665. https://doi.org/10.1016/j.epsl.2022.117665

Fantle, M.S., Tipper, E.T. (2014) Calcium isotopes in the global biogeochemical Ca cycle: Implications for development of a Ca isotope proxy. *Earth-Science Reviews* 129, 148–177. https://doi.org/10.1016/j.earscirev.2013.10.004

Feng, C., Qin, T., Huang, S., Wu, Z., Huang, F. (2014) First-principles investigations of equilibrium calcium isotope fractionation between clinopyroxene and Ca-doped orthopyroxene. *Geochimica et Cosmochimica Acta* 143, 132–142. https://doi.org/10.1016/j.gca.2014.06.002

Foley, S.F., Pintér, Z. (2018) *Primary melt compositions in the earth's mantle*. In: Kono, Y. and Sanloup, C. (Eds.) Magmas Under Pressure: Advances in High-Pressure Experiments on Structure and Properties of Melts, 3-42. Elsevier. https://doi.org/10.1016/B978-0-12-811301-1.00001-0

Garrity, K.F., Bennett, J.W., Rabe, K.M., Vanderbilt, D. (2014) Pseudopotentials for high-throughput DFT calculations. *Computational Materials Science* 81, 446-452. https://doi.org/10.1016/j.commatsci.2013.08.053

Giannozzi, P. Baroni, S., Bonini, N., Calandra, M., Car, R., Cavazzoni, C., Ceresoli, D., Chiarotti, G.L., Cococcioni, M., Dabo, I. and Dal Corso, A. (2009) QUANTUM ESPRESSO: A modular and open-source software project for quantum simulations of materials. *Journal of Physics Condensed Matter* 21, 395502. https://doi.org/10.1088/0953-8984/21/39/395502

Griffith, E.M., Schauble, E.A., Bullen, T.D., Paytan, A. (2008) Characterization of calcium isotopes in natural and synthetic barite. *Geochimica et Cosmochimica Acta* 72, 5641–5658. https://doi.org/10.1016/j.gca.2008.08.010

Harmer, R.E., Gittins, J. (1998) The case for primary, mantle-derived carbonatite magma. *Journal of Petrology* 39, 1895–1903. https://doi.org/10.1093/petroj/39.11-12.1895

He, Y., Wang, Y., Zhu, C., Huang, S., Li, S. (2017) Mass-independent and mass-dependent Ca isotopic compositions of thirteen geological reference materials measured by thermal ionisation mass spectrometry. *Geostandards and Geoanalytical Research* 41, 283–302. https://doi.org/10.1111/ggr.12153

Hin, R.C., Schmidt, M.W., Bourdon, B. (2012) Experimental evidence for the absence of iron isotope fractionation between metal and silicate liquids at 1GPa and 1250–1300°C and its cosmochemical consequences. *Geochimica et Cosmochimica Acta* 93, 164–181. https://doi.org/10.1016/j.gca.2012.06.011

Huang, F., Zhou, C., Wang, W., Kang, J., Wu, Z. (2019) First-principles calculations of equilibrium Ca isotope fractionation: Implications for oldhamite formation and evolution of lunar magma ocean. *Earth and Planetary Science Letters* 510, 153–160. https://doi.org/10.1016/j.epsl.2018.12.034

Hulett, S.R.W., Simonetti, A., Rasbury, E.T., Hemming, N.G. (2016) Recycling of subducted crustal components into carbonatite melts revealed by boron isotopes. *Nature Geoscience* 9, 904–908. https://doi.org/10.1038/ngeo2831

Ionov, D.A., O'Reilly, S.Y., Genshaft, Y.S., Kopylova, M.G. (1996) Carbonate-bearing mantle peridotite xenoliths from Spitsbergen: Phase relationships, mineral compositions and trace-element residence. *Contributions to Mineralogy and Petrology* 125, 375–392. https://doi.org/10.1007/s004100050229

Johnson, C.M., Bell, K., Beard, B.L., Shultis, A.I. (2010) Iron isotope compositions of carbonatites record melt generation,

crystallization, and late-stage volatile-transport processes. *Mineralogy and Petrology* 98, 91–110. https://doi.org/10.1007/s00710-009-0055-4

Kang, J.T., Zhou, C., Huang, J.Y., Hao, Y.T., Liu, F., Zhu, H.L., Zhang, Z.F., Huang, F. (2020) Diffusion-driven Ca-Fe isotope fractionations in the upper mantle: Implications for mantle cooling and melt infiltration. *Geochimica et Cosmochimica Acta* 290, 41–58. https://doi.org/10.1016/j.gca.2020.08.033

Kang, J.T., Ionov, D.A., Liu, F., Zhang, C.L., Golovin, A. V., Qin, L.P., Zhang, Z.F., Huang, F. (2017) Calcium isotopic fractionation in mantle peridotites by melting and metasomatism and Ca isotope composition of the Bulk Silicate Earth. *Earth and Planetary Science Letters* 474, 128–137. https://doi.org/10.1016/j.epsl.2017.05.035

Kuebler, C., Simonetti, A., Chen, W., Simonetti, S.S. (2020) Boron isotopic investigation of the Bayan Obo carbonatite complex: Insights into the source of mantle carbon and hydrothermal alteration. *Chemical Geology* 557, 119859. https://doi.org/10.1016/j.chemgeo.2020.119859

Lee, W.-J., Wyllie, P.J. (1998) Petrogenesis of Carbonatite Magmas from Mantle to Crust, Constrained by the System CaO-(MgO + FeO*)-(Na$_2$O + K$_2$O)-(SiO$_2$ + Al$_2$O$_3$ + TiO$_2$)-CO$_2$. *Journal of Petrology* 39, 495–517. https://doi.org/10.1093/petroj/39.3.495

Li, Y., Wu, Z., Huang, S., Wang, W. (2022) Pressure and concentration effects on intermineral calcium isotope fractionation involving garnet. *Chemical Geology* 591, 120722. https://doi.org/10.1016/j.chemgeo.2022.120722

Li, W.Y., Yu, H.M., Xu, J., Halama, R., Bell, K., Nan, X.Y., Huang, F. (2020) Barium isotopic composition of the mantle: Constraints from carbonatites. *Geochimica et Cosmochimica Acta* 278, 235–243. https://doi.org/10.1016/j.gca.2019.06.041

Li, W.Y., Teng, F.Z., Halama, R., Keller, J., Klaudius, J. (2016) Magnesium isotope fractionation during carbonatite magmatism at Oldoinyo Lengai, Tanzania. *Earth and Planetary Science Letters* 444, 26–33. https://doi.org/10.1016/j.epsl.2016.03.034

Lu, W.-N., He, Y., Wang, Y., Ke, S. (2019) Behavior of calcium isotopes during continental subduction recorded in meta-basaltic rocks. *Geochimica et Cosmochimica Acta* 278, 392-404. https://doi.org/10.1016/j.gca.2019.09.027

Marschall, H.R. (2018) Boron isotopes in the ocean floor realm and the mantle. In: Marschall, H., Foster, G. (Eds.) Boron isotopes: The fifth element. Advances in Isotope Geochemistry. Springer, 189-215. https://doi.org/10.1007/978-3-319-64666-4_8

Martin, L.H.J., Schmidt, M.W., Mattsson, H.B., Guenther, D. (2013) Element Partitioning between Immiscible Carbonatite and Silicate Melts for Dry and H2O-bearing Systems at 1-3gpa. *Journal of Petrology* 54, 2301–2338. https://doi.org/10.1093/petrology/egt048

Méheut, M., Lazzeri, M., Balan, E., Mauri, F. (2007) Equilibrium isotopic fractionation in the kaolinite, quartz, water system: Prediction from first-principles density-functional theory. *Geochimica et Cosmochimica Acta* 71, 3170–3181. https://doi.org/10.1016/j.gca.2007.04.012

Mills, J. V., DePaolo, D.J., Lammers, L.N. (2021) The influence of Ca:CO$_3$ stoichiometry on Ca isotope fractionation: Implications for process-based models of calcite growth. *Geochimica et Cosmochimica Acta* 298, 87–111. https://doi.org/10.1016/j.gca.2021.01.016

Mitchell, R.H., Gittins, J. (2022) Carbonatites and carbothermalites: A revised classification. *Lithos* 430–431, 106861. https://doi.org/10.1016/j.lithos.2022.106861

Momma, K., Izumi, F. (2011) VESTA 3 for three-dimensional visualization of crystal, volumetric and morphology data. *Journal of Applied Crystallography* 44, 1272–1276. https://doi.org/10.1107/S0021889811038970

Morizet, Y., Paris, M., Gaillard, F., Scaillet, B. (2014) Carbon dioxide in silica-undersaturated melt. Part I: The effect of mixed alkalis (K and Na) on CO2 solubility and speciation. *Geochimica et Cosmochimica Acta* 141, 45–61. https://doi.org/10.1016/j.gca.2014.06.014

Morizet, Y., Brooker, R.A., Kohn, S.C. (2002) CO2 in haplo-phonolite melt: solubility, speciation and carbonate complexation. *Geochimica et Cosmochimica Acta* 66, 1809–1820. https://doi.org/10.1016/S0016-7037(01)00893-6

Perdew, J.P., Burke, K., Ernzerhof, M. (1996) Generalized Gradient Approximation Made Simple. *Physical Review Letters* 77, 3865–3868. https://doi.org/10.1103/PhysRevLett.77.3865

Pirajno, F., González-Álvarez, I., Chen, W., Kyser, K.T., Simonetti, A., Leduc, E., leGras, M. (2014) The Gifford Creek Ferrocarbonatite Complex, Gascoyne Province, Western Australia: Associated fenitic alteration and a putative link with the ~1075Ma Warakurna LIP. *Lithos* 202–203, 100–119. https://doi.org/10.1016/j.lithos.2014.05.012

Russell, W.A.A., Papanastassiou, D.A.A., Tombrello, T.A.A. (1978) Ca isotope fractionation on the Earth and other solar system materials. *Geochimica et Cosmochimica Acta* 42, 1075–1090. https://doi.org/10.1016/0016-7037(78)90105-9

Sartori, G., Galli, A., Weidendorfer, D., Schmidt, M.W. (2023) A tool to distinguish magmatic from secondarily recrystallized carbonatites—Calcite/apatite rare earth element partitioning. *Geology* 51, 54–58. https://doi.org/10.1130/G50416.1

Sartori, G., Schmidt, M.W. (2023) Phosphorous-solubility in carbonatite melts: Apatite crystallization modeled via its solubility product. *Geochimica et Cosmochimica Acta* 352, 122–132. https://doi.org/10.1016/j.gca.2023.04.034

Saunderson, D.H., Peckham, G.E. (1971) The lattice dynamics of calcium oxide. *Journal of Physics C: Solid State Physics 4, 209*. https://doi.org/10.1088/0022-3719/4/14/016

Schauble, E.A. (2011) First-principles estimates of equilibrium magnesium isotope fractionation in silicate, oxide, carbonate and hexaaquamagnesium(2+) crystals. *Geochimica et Cosmochimica Acta* 75, 844–869. https://doi.org/10.1016/j.gca.2010.09.044

Schauble, E.A., Ghosh, P., Eiler, J.M. (2006) Preferential formation of 13C–18O bonds in carbonate minerals, estimated using first-principles lattice dynamics. *Geochimica et Cosmochimica Acta* 70, 2510–2529. https://doi.org/10.1016/j.gca.2006.02.011

Schmidt, M.W., Weidendorfer, D. (2018) Carbonatites in oceanic hotspots. *Geology* 46, 435–438. https://doi.org/10.1130/G39621.1

Schmidt, M.W., Connolly, J.A.D., Günther, D., Bogaerts, M. (2006) Element partitioning: The role of melt structure and composition. *Science* 312, 1646–1650. https://doi.org/10.1126/science.1126690

Smith, H.J., Spivack, A.J., Staudigel, H., Hart, S.R. (1995) The boron isotopic composition of altered oceanic crust. *Chemical Geology* 126, 119–135. https://doi.org/10.1016/0009-2541(95)00113-6

Smith, C.B., Haggerty, S.E., Chatterjee, B., Beard, A., and Townend, R. (2013) Kimberlite, lamproite, ultramafic lamprophyre, and carbonatite relationships on the Dharwar Craton, India; an example from the Khaderpet pipe, a diamondiferous ultramafic with associated carbonatite intrusion. *Lithos*, *182*, 102-113. https://doi.org/10.1016/j.lithos.2013.10.006

Soderman, C.R., Shorttle, O., Matthews, S., Williams, H.M. (2022) Global trends in novel stable isotopes in basalts: Theory and observations. *Geochimica et Cosmochimica Acta* 318, 388–414. https://doi.org/10.1016/j.gca.2021.12.008

Song, Y., Li, Y., Wang, W., Wu, Z. (2019) First-principles investigation of the concentration effect on equilibrium fractionation of Ca isotopes in forsterite. *Acta Geochimica* 38, 497–507. https://doi.org/10.1007/s11631-019-00346-w

Su, B.X., Hu, Y., Teng, F.Z., Xiao, Y., Zhang, H.F., Sun, Y., Bai, Y., Zhu, B., Zhou, X.H., Ying, J.F. (2019) Light Mg isotopes in mantle-derived lavas caused by chromite crystallization, instead of carbonatite metasomatism. *Earth and Planetary Science Letters* 522, 79–86. https://doi.org/10.1016/j.epsl.2019.06.016

Sun, J., Zhu, X.K., Belshaw, N.S., Chen, W., Doroshkevich, A.G., Luo, W.J., Song, W.L., Chen, B.B., Cheng, Z.G., Li, Z.H., Wang, Y. (2021) Ca isotope systematics of carbonatites: Insights into carbonatite source and evolution. *Geochemical Perspectives Letters* 17, 11–15. https://doi.org/10.7185/geochemlet.2107

Tang, J., Köhler, S.J., Dietzel, M. (2008) Sr^{2+}/Ca^{2+} and $^{44}Ca/^{40}Ca$ fractionation during inorganic calcite formation: I. Sr incorporation. *Geochimica et Cosmochimica Acta* 72, 3718–3732. https://doi.org/10.1016/j.gca.2008.05.031

Tappe, S., Romer, R. L., Stracke, A., Steenfelt, A., Smart, K. A., Muehlenbachs, K., and Torsvik, T. H. (2017) Sources and mobility of carbonate melts beneath cratons, with implications for deep carbon cycling, metasomatism and rift initiation. *Earth and Planetary Science Letters*, *466*, 152-167. https://doi.org/10.1016/j.epsl.2017.03.011

Urey, H.C. (1947) The thermodynamic properties of isotopic substances. *Journal of the Chemical Society (Resumed)* 562. https://doi.org/10.1039/jr9470000562

Veksler, I. V., Dorfman, A.M., Dulski, P., Kamenetsky, V.S., Danyushevsky, L. V., Jeffries, T., Dingwell, D.B. (2012) Partitioning of elements between silicate melt and immiscible fluoride, chloride, carbonate, phosphate and sulfate melts, with implications to the origin of natrocarbonatite. *Geochimica et Cosmochimica Acta* 79, 20–40. https://doi.org/10.1016/j.gca.2011.11.035

Vils, F., Tonarini, S., Kalt, A., Seitz, H.-M. (2009) Boron, lithium and strontium isotopes as tracers of seawater–serpentinite interaction at Mid-Atlantic ridge, ODP Leg 209. *Earth and Planetary Science Letters* 286, 414–425. https://doi.org/10.1016/j.epsl.2009.07.005

Walter, B.F., Giebel, R.J., Steele-MacInnis, M., Marks, M.A.W., Kolb, J., Markl, G. (2021) Fluids associated with carbonatitic magmatism: A critical review and implications for carbonatite magma ascent. *Earth-Science Reviews* 215, 103509. https://doi.org/10.1016/j.earscirev.2021.103509

Wang, W., Kang, J., Huang, F. (2023) How precise and how accurate can magnesium isotope analysis be by the sample-standard bracketing method? *International Journal of Mass Spectrometry* 491, 117102. https://doi.org/10.1016/j.ijms.2023.117102

Wang, W., Qin, T., Zhou, C., Huang, S., Wu, Z., Huang, F. (2017a) Concentration effect on equilibrium fractionation of Mg-Ca isotopes in carbonate minerals: Insights from first-principles calculations. *Geochimica et Cosmochimica Acta* 208, 185–197. https://doi.org/10.1016/j.gca.2017.03.023

Wang, W., Zhou, C., Qin, T., Kang, J.T., Huang, S., Wu, Z., Huang, F. (2017b) Effect of Ca content on equilibrium Ca isotope fractionation between orthopyroxene and clinopyroxene. *Geochimica et Cosmochimica Acta* 219, 44–56. https://doi.org/10.1016/j.gca.2017.09.022

Watkins, J.M., Antonelli, M.A. (2021) Beyond equilibrium: kinetic isotope fractionation in high-temperature environments. *Elements* 17, 383–388. https://doi.org/10.2138/gselements.17.6.383

Weidendorfer, D., Asimow, P.D. (2022) Experimental constraints on truly conjugate alkaline silicate – carbonatite melt pairs. *Earth and Planetary Science Letters* 584, 117500. https://doi.org/10.1016/j.epsl.2022.117500

Weidendorfer, D., Schmidt, M.W., Mattsson, H.B. (2017) A common origin of carbonatite magmas. *Geology* 45, 507–510. https://doi.org/10.1130/G38801.1

Weidendorfer, D., Schmidt, M.W., Mattsson, H.B. (2016) Fractional crystallization of Si-undersaturated alkaline magmas leading to unmixing of carbonatites on Brava Island (Cape Verde) and a general model of carbonatite genesis in alkaline magma suites. *Contributions to Mineralogy and Petrology* 171, 1–29. https://doi.org/10.1007/s00410-016-1249-5

Woolley, A.R., and Kjarsgaard, B.A. (2008) Carbonatite occurrences of the world: map and database. *Geological Survey Canada Open File 5796.* https://doi.org/10.4095/225115

Xiao, Z.-C., Zhou, C., Kang, J.-T., Wu, Z.-Q., Huang, F. (2022) The factors controlling equilibrium inter-mineral Ca isotope fractionation: Insights from first-principles calculations. *Geochimica et Cosmochimica Acta* 333, 373–389. https://doi.org/10.1016/j.gca.2022.07.021

Yamaoka, K., Ishikawa, T., Matsubaya, O., Ishiyama, D., Nagaishi, K., Hiroyasu, Y., Chiba, H., Kawahata, H. (2012) Boron and oxygen isotope systematics for a complete section of oceanic crustal rocks in the Oman ophiolite. *Geochimica et Cosmochimica Acta* 84, 543–559. https://doi.org/10.1016/j.gca.2012.01.043

Yamaoka, K., Matsukura, S., Ishikawa, T., Kawahata, H. (2015) Boron isotope systematics of a fossil hydrothermal system from the Troodos ophiolite, Cyprus: Water-rock interactions in the oceanic crust and subseafloor ore deposits. *Chemical Geology* 396, 61–73. https://doi.org/10.1016/j.chemgeo.2014.12.023

Yaxley, G.M., Brey, G.P. (2004) Phase relations of carbonate-bearing eclogite assemblages from 2.5 to 5.5 GPa: Implications for petrogenesis of carbonatites. *Contributions to Mineralogy and Petrology* 146, 606–619. https://doi.org/10.1007/s00410-003-0517-3

Zhao, K., Dai, L.Q., Fang, W., Zheng, Y.F., Zhao, Z.F., Zheng, F. (2022) Decoupling between Mg and Ca isotopes in alkali basalts: Implications for geochemical differentiation of subduction zone fluids. *Chemical Geology* 606, 120983. https://doi.org/10.1016/j.chemgeo.2022.120983

Zhao, X., Zhang, Z., Huang, S., Liu, Y., Li, X., Zhang, H. (2017) Coupled extremely light Ca and Fe isotopes in peridotites. *Geochimica et Cosmochimica Acta* 208, 368–380. https://doi.org/10.1016/j.gca.2017.03.024

Zhu, H., Liao, R., Liu, H., Du, L., Li, H., Li, C., Zhang, Z., Sun, W. (2021) Calcium isotopic fractionation during magma differentiation: Constraints from volcanic glasses from the eastern Manus Basin. *Geochimica et Cosmochimica Acta* 305, 228–242. https://doi.org/10.1016/j.gca.2021.05.032